ELECTROCHEMICAL DETECTION AND TOTAL INTERNAL REFLECTION FLUORESCENCE MICROSCOPY: ILLUMINATING THE EXOCYTOTIC MECHANISM

A Dissertation

Presented to the Faculty of the Graduate School

of Cornell University

In Partial Fulfillment of the Requirements for the Degree of

Doctor of Philosophy

by

Kassandra Juliet Kisler Elliott

August 2009

ELECTROCHEMICAL DETECTION AND TOTAL INTERNAL REFLECTION FLUORESCENCE MICROSCOPY: ILLUMINATING THE EXOCYTOTIC MECHANISM

Kassandra Juliet Kisler Elliott, Ph. D.

Cornell University 2009

Exocytosis is an essential cellular process wherein membrane-bound packets, or vesicles, of neurotransmitter or hormone molecules are released into the extracellular space. Exocytosis is the method by which neurons communicate with one another at synapses, how molecules such as histamines and adrenaline are released into the bloodstream, and even how cells carry cargo from one intracellular compartment to another. Dysfunction of the exocytotic process is implicated in various neurological disorders such as Parkinson's disease and schizophrenia, and exposure to Tetanus and Botulism toxins. While exocytosis continues to be extensively studied, and links to diseases and toxins such as those mentioned above have been made, much of the molecular mechanism that enables exocytosis remains a mystery.

In this dissertation, I will attempt to illuminate some small pieces of this mystery using electrochemical detection techniques, often in combination with Total Internal Reflection Fluorescence (TIRF) microscopy. Microelectrode array devices were fabricated to electrochemically detect release of transmitter molecules from vesicles amperometrically. Amperometry is a technique where an electrode held near a cell at a positive potential will oxidize molecules released from vesicles, generating a transient current spike. Fluorescent labels in the cell could be monitored simultaneously via TIRF microscopy, which excites fluorophores in only a thin layer

above a coverslip.

In the chapters that follow, I describe the construction of an Annular TIRF microscope. I will explore the kinetics of exocytotic events, were it was found that release of vesicular contents is fast, but diffusion of the released molecules near the cell surface was slower then expected, in contrast to what was previously believed. Then, I will detail the development and use of transparent microelectrodes in combination with TIRF microscopy to observe exocytosis *through* electrodes. Next I will study the effects of the addition of charged residues to the C-terminus of synaptobrevin II, a vesicle membrane protein essential for exocytosis. The addition of these charged residues inhibited exocytosis, leading to new hypotheses about the function of synaptobrevin II in the exocytotic process. Finally, I report the interaction of suspended carbon nanotubes with cell membranes, which has implications for novel cell biosensors.

BIOGRAPHICAL SKETCH

The oldest of five children, Kassandra was born and raised in "Silicon Valley," Santa Clara Valley, California. She was homeschooled until the age of 14, when she started taking courses at San Jose City College. Kassandra received her AA in Physics, with Honors, from San Jose City College in 1996, then transferred to the University of California at Davis to pursue dual degrees in Physics and Chemistry (because she just couldn't decide between the two, and they were so much fun!). Later, Kassandra found that the Physics Department's Applied Physics curriculum was more in line with her scientific interests, and changed her major to reflect that.

After a brief hiatus due to the birth of her oldest son, Marcus, she returned to UC Davis and completed her BS in Applied Physics (with a Materials Science emphasis) and BA in Chemistry (both with honors) in 1999. She was awarded the UC Davis Saxon-Patton Prize in Physics the same year. Along the way, she spent summers characterizing semiconductor thin films using scanning probe microscopy at Arizona State University in Tempe, and fabricated and analyzed polymer light emitting diodes at UC Santa Cruz. After graduation, she spent a year and a half as a manufacturing engineer at Coherent, Inc., working with frequency doubling crystals for their laser systems.

2001 was a particularly eventful year for Kassandra, as she married Jamison Elliott, her second child, Tryphena, was born, and she began grad school at Cornell University, making the journey from California cross-country in her beloved little blue Saturn. At Cornell, an odd series of events and a healthy dose of serendipity landed her in Manfred Lindau's lab in the School of Applied Physics at Cornell, where her education in biological sciences, microscopy, and nanofabrication began. Now with a third child in tow, Aleric, she looks forward to the completion of her PhD in Applied Physics, and what ever adventures and challenges lay ahead.

In memory of my grandfathers, Floyd Kisler and Alfred Mikelich

To my children, Marcus, Tryphena, and Aleric

and to Jamison, *with love always*

Science is no less magical then magic, it is just repeatable.

- Louis J DeFelice

ACKNOWLEDGMENTS

Oh, boy. Where to begin? There are so many people who have done so many little things over the years that I'm sure I'll miss some of you, but I thank you nonetheless, and apologize if I missed mentioning you by name.

At San Jose City College, I recall learning geology and astronomy from Mr. Martin's tough but fascinating classes, and my first exciting experiences with physics and chemistry with Dr. Ibarra, Dr. Song, and Mr. Brown. Then there was Ms. Kendall, who between her and my mother drilled into my head (but in a fun sort of way) how to write an English paper. But I still can't spell.

From my time at UC Davis, I am thankful to all my fellow students in my physics courses. There we were, that first quarter of our junior year in physics. Most of us transfer students who had no clue what we were getting ourselves into, we banded together into a network of homework buddies and friends, calling and gathering together at all hours of the night to get our homework done, and occasionally getting out to have a little fun. I had great friends in chemistry too. I particularly remember all the fun we had with liquid nitrogen and blowing things up for our chemistry demos (all chemists are pyros), and eating our way through the ACS national meeting in San Francisco. Then there were all the cool professors in physics and chemistry, who always kept things interesting. Particularly Professor Reid, who had a wealth of knowledge and wisdom, and sent me science books to read when I took time off after the birth of my son.

The summer I spent working for Sue Carter at UC Santa Cruz was a great experience. Sue's advice is what really catalyzed my effort to go to grad school, and pointed me towards Cornell.

I survived my first year at Cornell with the assistance of my fellow Applied

Physics first year grads, all of us crammed into one tiny office space trying to master Persis Drell's quantum mechanics and Jim Sethna's statistical mechanics in between our teaching assignments.

I am grateful to Manfred Lindau for inviting me into his lab and allowing me to learn, to create, and to discover. For the guidance, and for his patience in dealing with my family issues over the years. Learning about exocytosis, and trying to tease out details of how it works has been a challenging, exciting, and in the end rewarding experience. I also want to thank my committee members, Lois Pollack and George Malliaras, for their advice and guidance during my time at Cornell.

It has been wonderful working with the members of the Lindau Lab over the years. I have learned much from my fellow lab mates, and I hope I have passed on some of what I have learned to the newer members of the lab. I am particularly indebted to Ismail Hafez, who was there at the beginning and taught me a lot of the basics, and Khajak Berberian who worked with me on many of the projects I did in the lab, and with whom I would often discuss ideas, problems, and solutions. And to Joan Lenz, who does so much to make it possible for the rest of us to focus on the research. Then there are Brian, Ying, Mark, and Alycia, whose questions keep me on my toes. Sunitha, who was a good friend, Annita, a wonderful collaborator and scientist, and Qinghua, a very capable scientist, and together with Khajak a constant source of entertainment.

During my time here, I also had the opportunity to collaborate with Lisa Larrimore and Samantha Roberts from Paul McEuen's group in the Physics department. I have had a great time working with Sam and Lisa and learning about carbon nanotubes. I would like to thank Paul McEuen for allowing the project to continue despite all the setbacks we have encountered.

I would also like to thank all the support staff in the Applied Physics offices

for their assistance, advice, and occasional cheering-up during my time here. To the people at the Cornell Nanofabrication Facility, the Nanobiotechnology Center, the Cornell Center for Materials Research, and Center for Nanoscale Systems for their support and the opportunity to use all those cool tools they have. And for the occasional lunch. To Nev and Kevin and the rest of the staff in the CCMR outreach program for the opportunity to get the next generation excited about science. I think I had as much fun doing the demos as the kids I was teaching. The free food was nice too, and always appreciated.

To my parents, Carol and Doyle, who provided encouragement, advice, a good home, and a little financial assistance when I needed it. And who were two of the few people who didn't say "are you crazy?!" when I decided to double major in chemistry and physics. To my siblings, Christopher, Gretchen, Isabeau and Colin, who always made life interesting at home. I am particularly grateful to Gretchen and Isabeau for keeping a very young Marcus in line. I am also thankful for Kathy Lovejoy and her family. She is one of the best things that has happened to us since we came to Ithaca, and over the years she has become something of an honorary grandmother to my children.

And finally, my children, Marcus, Tryphena, and Aleric, who were often the first to see my presentations and ask questions (and they *did* ask questions!). And for all the patience they could muster while mommy spent so much time with her computer. I finally did get a little work done. And to Jamison, for keeping me sane, reminding me to eat and sleep, and a million other things. Who knew where I was going, and married me anyway.

- KKE

Ithaca and Groton NY, June 2009

TABLE OF CONTENTS

LIST OF FIGURES

LIST OF TABLES

LIST OF ABBREVIATIONS

AFM ...……...…….Atomic Force Microscope

Da ...……...……Dalton, mass of one H atom ($1.66x10^{-24}$g)

CNT ...……..Carbon Nanotube

ECD ...……...……..Electrochemical Detector (Array)

GFP ...…….Green Fluorescent Protein

MUNC-18 ...……Mammalian homologue of UNC-18

NA ...……...…..Numerical Aperture

SNAP-25 ……...…… Synaptosome-Associated Protein of 25 kDa

SNARE ...…Soluble N-ethylmaleimide-Sensitive Factor Attachment Protein Receptor

SybII ……...…….Synaptobrevin II (or 2)

TIRF ……...…Total Internal Reflection Fluorescence

WT ……..……Wild-Type

CHAPTER 1

INTRODUCTION

1.1 Neuronal Communication: The Neuron Says 'Hello'

Cell to cell communication is a vital function of living things. One of the most important forms of intercellular communication is from neuron to neuron and from neurons to other cells in the body. Signals from neuron to neuron, or neuron to cell are most often carried by small molecules, or neurotransmitters, released from the neuron, and "received" via receptors in the target cell membrane (Alberts, Bray et al. 1989). Inside the neuron, neurotransmitter molecules are kept in membrane-bound packets, or vesicles, awaiting the signal to fuse with the cell membrane and release the transmitter molecules. The process of vesicle fusion and transmitter release is termed exocytosis. (Figure 1). Many details of the exocytotic mechanism remain a mystery, although dysfunction of the exocytotic process is implicated in diseases such as Parkinson's (Cragg, Baufreton et al. 2004), schizophrenia (Johnson, Oliver et al. 2008), and exposure to tetanus and botulism toxins (Montecucco and Schiavo 1994).

In this chapter I will introduce some of the basic biological information and exocytotic detection methods that will be used throughout this work to help unravel the mechanism of exocytosis.

1.2 Chromaffin Cells as a Model System for Exocytosis

In the chapters that follow, the data presented was obtained from chromaffin cells, so named because they are readily stained with chromium compounds (Coupland 1965). In addition to neurons, chromaffin cells of the adrenal gland release hormones (adrenaline and noradrenaline mainly) via exocytosis, as do many other hormone secreting cell types. Chromaffin cells are considered to be closely related to neurons,

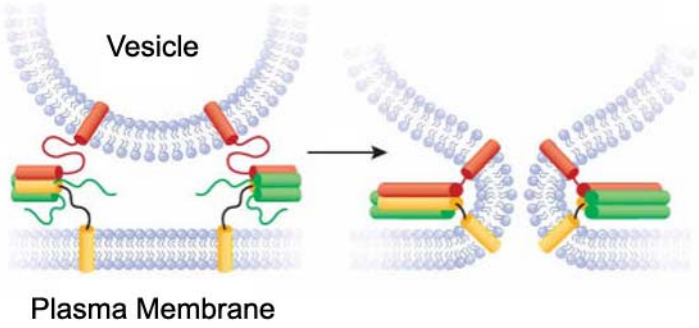

Figure 1.1. The exocytotic process. Left: a vesicle approaches the plasma membrane and fusion proteins begin to interact with each other (colored sausages represent structured portions of the proteins). Right: upon stimulation, the fusion proteins "zip up," pulling the vesicle and plasma membranes together and creating a fusion pore. This pore usually expands to release the contents of the vesicle into the extracellular space. Modified from Nat Struct Mol Biol. 2008 July; 15(7): 665–674.

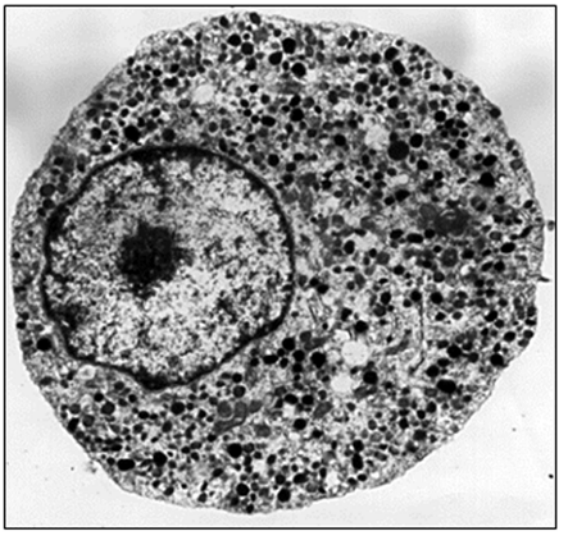

Figure 1.2. An electron micrograph of a slice through a chromaffin cell. Large circular region on the left is the nucleus. Small dark spots are individual dense core vesicles. Micrograph from Horstmann and Lindau, unpublished.

receiving signals directly from neurons and are considered part of the sympathetic nervous system (Coupland 1965). Chromaffin cells are widely used as a model to study neurosecretion because they employ the same proteins in exocytosis as neurons, but are easier to culture and acquire data from than neurons. At a typical neuron synapse there may be about 50 vesicles or so, each on the order of 50 nm in diameter. Chromaffin cells, on the other hand, contain thousands of vesicles, each on the order of 300 nm across (Figure 1.2). In methods that depend on detecting molecules or visual observation – both of which will be employed in the following chapters – chromaffin cells are better suited.

1.3 The SNARE Proteins

Many proteins have an influence on the exocytotic process, from the ubiquitous actin filaments (Burgoyne and Cheek 1987; Cheek and Burgoyne 1987; Berberian, Torres et al. 2009) to the more colorfully named MUNC-18 (mammalian homologue of UNC-18[*]) (Voets, Toonen et al. 2001; Schutz, Zilly et al. 2005). Within this pool of proteins that affect exocytosis, Syntaxin 1, SNAP-25 (synaptosome-associated protein of 25 kDa), and Synaptobrevin 2, collectively called the SNARE (soluble N-ethylmaleimide-sensitive factor attachment protein receptor) complex, are essential to the exocytotic mechanism. Indeed, cleavage of any one of these proteins by either tetanus or botulism toxin severely impairs or abolishes exocytosis (Montecucco and Schiavo 1994).

SNAP-25 and syntaxin are both located in the plasma membrane of the cell, and synaptobrevin is found on the vesicle membrane. Syntaxin and synaptobrevin are each anchored into their respective membranes via single transmembrane regions at

[*] UNC-18, UNCoordinated locomotion protein 18, is a protein in C. Elegans that when mutated causes paralysis. Brenner, S. (1974). "The genetics of Caenorhabditis elegans." Genetics **77**(1): 71-94.

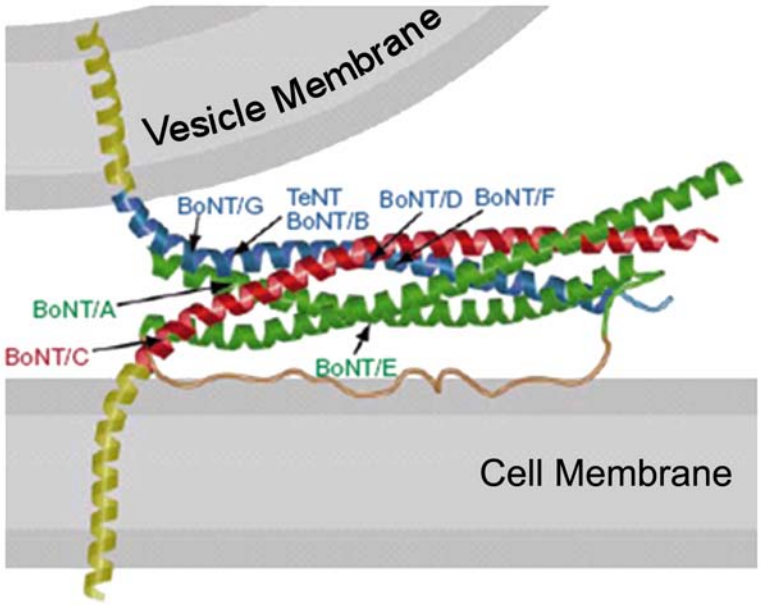

Figure 1.3. The SNARE complex is composed of three proteins: Syntaxin (red), synaptobrevin (blue), and SNAP-25 (green). The transmembrane domains of Syntaxin and Synaptobrevin are shown in yellow. When the vesicle is close to the cell membrane, the three proteins coil into a helical structure, drawing the two membranes together. Image adapted from R. B. Sutton, et al, Nature, September 14,1998.

their C-termini, while SNAP-25 is attached to the plasma membrane in its central region via palmitoylation (covalent attachment to lipids in the membrane). When a vesicle is near the plasma membrane, these three proteins interact to form a four helix coiled-coil motif (with SNAP-25 folding something like a paperclip to contribute two alpha helices) as shown in Figure 1.**3**, with toxin cleavage sites indicated (Sutton, Fasshauer et al. 1998). The motif forms relatively loosely at first, with the N-terminal end more tightly formed then the C-terminal end. On stimulation, and presumably with the aid of periphery proteins, the motif tightens up, or ”zips,” from the N- to C-terminus (Sorensen, Wiederhold et al. 2006). This action is believed to be what somehow initiates the fusion between the vesicle and plasma membranes.

1.4 Amperometry

A unique feature of some catecholamines, adrenaline and noradrenaline among them, is their ability to be oxidized. This property makes it possible to use an electrochemical technique called amperometry to detect these molecules as they are released from cells (Wightman, Jankowski et al. 1991). In amperometry, an electrode (traditionally a carbon fiber microelectrode) is held at a positive potential and positioned against a cell of interest. When a release event occurs in the vicinity of the electrode, adrenaline molecules diffuse to the electrode. Upon contact with the electrode, the molecules are oxidized, with each molecule giving up two electrons to the electrode (Figure 1.4). The electrode detects these release events as transient current spikes. Quantities such as the spike charge or quantal size (area under the spike), its height, and its width provide information about the vesicle and how it was exocytosed. Figure 1.5 shows an example of an amperometric spike with parameters of interest indicated.

A feature often seen in at the beginning of amperometric spikes is the foot signal (Chow, Rüden et al. 1992): a small increase in current that occurs prior to the rapid increase in current of a spike, as shown in Figure 1.5. This slow trickle of current indicates the initial opening of a fusion pore between the vesicle and plasma membranes, on the order of 2 nm in diameter (Albillos, Dernick et al. 1997).

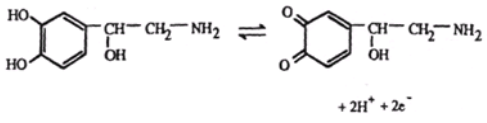

Figure 1.4. The oxidation of noradrenaline to its quinone form, releasing two electrons, and reverse reaction. From Single-Channel Recording, 2nd Ed. B. Sakmann and E. Neher, Eds. Plenum Press, NY 1995

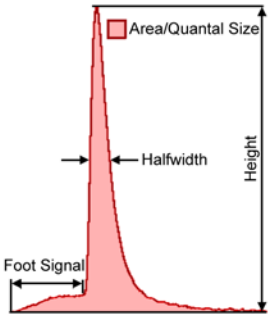

Figure 1.5. Amperometric event parameters of interest indicated on a sample event.

1.5 Amperometry on a Chip: Planar Microelectrode Arrays

Carbon fiber is not the only electrode material capable of detecting catecholamine molecules. Relatively nonreactive, polarizable metals such as platinum and gold can be used as well. We have fabricated and tested a variety of planar electrodes and electrode arrays for use as amperometric detectors of single exocytotic release events. In general, electrodes are fabricated on glass coverslips, with fused silica (SiO_2) or photoresist insulation (Figure 1.**6**). The advantage of fabricating the electrodes on glass is the ability to see through the coverslips to the cells above, and allows additional information about cell function to be recorded via brightfield or fluorescence microscopy simultaneously with the electrochemical measurements. In addition, I experimented with transparent conductive materials fabricated into electrode arrays.

1.6 Looking Ahead

The main goal of the research presented here has been to aid in the understanding of the exocytotic process and how the SNARE proteins function to induce exocytosis. A large part of the process has been the development of new tools and techniques to help

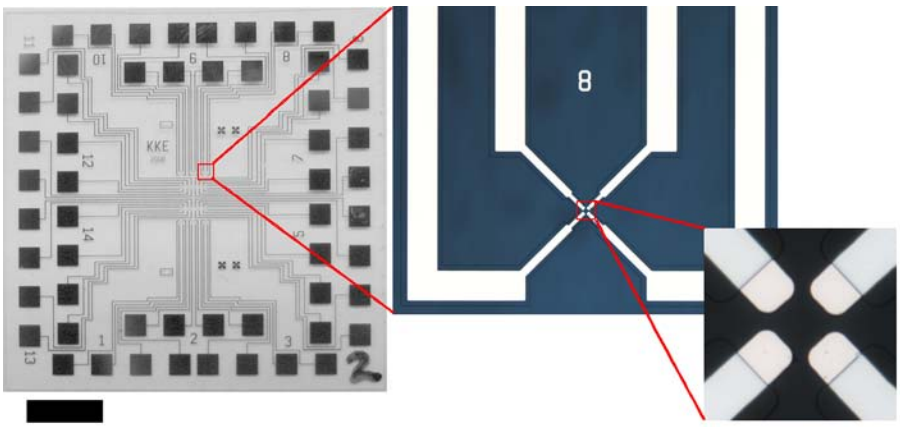

Figure 1.6. The latest version of the four-electrode ECD array. Left: Each coverslip has 14 sets of four electrodes. Scale bar is 5 mm. Center: An enlarged view of one electrode array. The widest part of the wires is 10 μm. Right: A further enlarged view showing the active electrode areas at the tips of the Pt wires. This device was insulated with SiO_2.

answer these questions. In the following chapters, I will discuss aspects of the creation and application of planar amperometric electrode techniques, microscopy techniques, and other novel cell detection methods, as well as the information gained using these methods.

In chapter 2, I will discuss the basics of total internal reflection fluorescence (TIRF) microscopy, a fluorescence technique used to excite fluorophores in a thin layer near the interface between a sample and a coverslip. Out-of-focus illumination is greatly reduced with this technique, which in turn enhances the signal to noise ratio. This property made it possible to image vesicular synaptobrevin mutant proteins in experiments described in chapter 5.

The first use of the electrochemical detector arrays in combination with fluorescence microscopy is demonstrated in chapter 3. The locations of release events on the cell surface could be determined electrochemically and correlated to

fluorescence signals, and information could be gained about the catecholamine release and diffusion kinetics with the aid of random walk simulations.

I will present the first use of transparent electrodes in combination with TIRF microscopy in chapter 4. These experiments include demonstrations of exocytosis of fluorescent dyes observed through the detecting electrodes of both a doped semiconductor material (indium tin oxide) and semitransparent gold films.

Chapter 5 describes experiments with cells expressing mutated synaptobrevin 2. The protein was mutated by the addition of charged peptides to the C-terminus of synaptobrevin 2, and the effects were investigated using TIRF microscopy and electrochemical detection. Addition of charged peptides has a strong inhibitory effect on exocytosis. This effect was somewhat surprising, and could have significant implications in our understanding of the exocytotic mechanism.

Chapter 6 digresses somewhat from the themes of the previous chapters. In this chapter I will look at the effects of interactions between carbon nanotubes and live cells. The goal of the research presented here being a more fundamental understanding of the effect of direct interaction of cell membrane with a carbon nanotube transistor in an aqueous environment.

Finally, I will summarize the research and discuss some future experiments in chapter 7.

REFERENCES

Alberts, B., D. Bray, et al. (1989). Molecular biology of the cell. New York, Garland Pub.

Albillos, A., G. Dernick, et al. (1997). "The exocytotic event in chromaffin cells revealed by patch amperometry." Nature **389**(6650): 509-12.

Berberian, K., A. J. Torres, et al. (2009). "F-actin and myosin II accelerate catecholamine release from chromaffin granules." J Neurosci **29**(3): 863-70.

Brenner, S. (1974). "The genetics of Caenorhabditis elegans." Genetics **77**(1): 71-94.

Burgoyne, R. D. and T. R. Cheek (1987). "Reorganisation of peripheral actin filaments as a prelude to exocytosis." Biosci Rep **7**(4): 281-8.

Cheek, T. R. and R. D. Burgoyne (1987). "Cyclic AMP inhibits both nicotine-induced actin disassembly and catecholamine secretion from bovine adrenal chromaffin cells." J Biol Chem **262**(24): 11663-6.

Chow, R. H., L. v. Rüden, et al. (1992). "Delay in vesicle fusion revealed by electrochemical monitoring of single secretory events in adrenal chromaffin cells." Nature **356**: 60-63.

Coupland, R. E. (1965). The Natural History of the Chromaffin Cell. London, Longmans, Green and Co.

Cragg, S. J., J. Baufreton, et al. (2004). "Synaptic release of dopamine in the subthalamic nucleus." Eur J Neurosci **20**(7): 1788-802.

Johnson, R. D., P. L. Oliver, et al. (2008). "SNARE proteins and schizophrenia: linking synaptic and neurodevelopmental hypotheses." Acta Biochim Pol **55**(4): 619-28.

Montecucco, C. and G. Schiavo (1994). "Mechanism of action of tetanus and botulinum neurotoxins." Mol Microbiol **13**(1): 1-8.

Schutz, D., F. Zilly, et al. (2005). "A dual function for Munc-18 in exocytosis of PC12 cells." Eur J Neurosci **21**(9): 2419-32.

Sorensen, J. B., K. Wiederhold, et al. (2006). "Sequential N- to C-terminal SNARE complex assembly drives priming and fusion of secretory vesicles." Embo J **25**(5): 955-66.

Sutton, R. B., D. Fasshauer, et al. (1998). "Crystal structure of a SNARE complex involved in synaptic exocytosis at 2.4 Å resolution." Nature **395**: 347-353.

Voets, T., R. F. Toonen, et al. (2001). "Munc18-1 promotes large dense-core vesicle docking." Neuron **31**(4): 581-91.

Wightman, R. M., J. A. Jankowski, et al. (1991). "Temporally resolved catecholamine spikes correspond to single vesicle release from individual chromaffin cells." Proceedings of the National Academy of Sciences of the United States of America **88**: 10754-10758.

CHAPTER 2

TOTAL INTERNAL REFLECTION FLUORESCENCE MICROSCOPY

2.1 Introduction

A key ingredient in the experiments presented in the following chapters is the use of Total Internal Reflection Fluorescence (TIRF) microscopy. TIRF microscopy involves shining excitation light onto a coverslip-sample interface at an oblique angle such that only fluorophores within about a hundred nanometers of the coverslip interface will be excited. The light emitted by those fluorophores is then collected by an objective. Total internal reflection (TIR) of light has been known for centuries. Indeed, Sir Isaac Newton was one of the first to describe TIR, recounting his observations of frustrated TIR between two slightly convex prisms (Newton 1952). TIR has been employed in many applications since that time, from periscopes and binoculars to optical fibers to material detection techniques such as TIR *spectroscopy*, a technique known to materials scientists for nearly 50 years (Mirabella 1993). The unique properties of TIR were first used to study a biological sample in the early 1980s, when Dr. Daniel Axelrod first affixed a prism to a coverslip full of fluorescently labeled cells, and excited them by shining a beam of light through the prism at just the right angle (Axelrod 1981). With many technological innovations since that first experiment, TIRF microscopy has blossomed into a highly useful and versatile research technique.

A major advantage of TIRF excitation is the ability to excite fluorophores in a very thin layer above the coverslip, typically on the order of 100-200 nm. For comparison, confocal microscopes, which basically function by blocking out all out-of-focus light using a small aperture or pin hole, can only achieve a minimum spot size of approximately 800 nm in the depth (z-) direction. And unlike TIRF microscopy, the spot must be scanned across the area of interest to generate an image.

Epifluorescence is worse yet, since excitation light can pass through the whole sample, degrading the signal-to-noise ratio due to an abundance of out-of-focus light.

In this chapter, I will present some of the basic concepts and calculations used in TIRF microscopy, and detail the design of the unique objective-based "Annular TIRF" microscope constructed for use in the Lindau Group laboratory.

2.2 Total Internal Reflection and the Evanescent Wave

Total internal refection (TIR) can occur when light travels from a medium of higher index of refraction (n_1) to a medium of lower index of refraction (n_2). Any light ray incident at the interface between the two media at an angle greater than the Critical Angle, θ_c, is totally reflected back into the first medium (glass in the example below). Hence the term "internal" in total internal reflection. From Snell's Law ($n_1 \sin\theta_1 = n_2 \sin\theta_2$, where θ_1 and θ_2 are the angles of incidence and refraction, respectively), the critical angle is given by:

$$\sin\theta_c = \frac{n_2}{n_1} \tag{2.1}$$

In classical ray optics, this would be the end of the story. But light is an electromagnetic wave (or particle -- your choice). In reality, a very small part of the light actually *does* make it into the second medium as an evanescent (decaying) wave. Interestingly, a calculation of Poynting's Vector, which I will not show here, would reveal no net energy flow into the second medium, as long as the light did not interact with anything else in that medium (Fornel 2001).

How rapidly the evanescent wave intensity decays with depth into the second medium is characterized by the penetration (or skin) depth, d_p. The intensity, I, in the second medium in a direction normal to the interface (Figure 2.1) has the form:

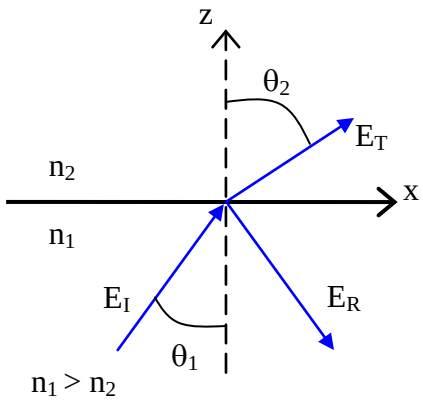

Figure 2.1. Coordinate system and light ray orientation for incident (E_I), reflected (E_R), and transmitted (E_T) light rays at the interface between more optically dense (n_1) and less optically dense (n_2) mediums.

$$I(z) = I_o \exp(-z/d_p) \tag{2.2}$$

where I_o is the intensity at the interface between the two materials.

The penetration depth can be easily derived using Snell's law and the equation for the transmitted electric field of the light wave. While the derivation is not particularly difficult, it is typically just hinted at in the literature (Born and Wolf 1970; Hecht and Zajñac 1987) or presented with little explanation (Oheim 2001). Therefore, I will present below a derivation of the evanescent field penetration depth. Assuming the coordinate system shown in Figure 2.1, the electric field wave in the second medium (transmitted wave) is given by:

$$E_T = E_{0T} \exp(i\vec{k} \cdot \vec{r} - i\omega t). \tag{2.3}$$

where $\vec{k}$ is the wave vector, $\vec{r}$ is the direction of propagation, ω the frequency, and t time. Looking at the $i\vec{k} \cdot \vec{r}$ term:

$$i\vec{k}\cdot\vec{r} = ik_z z + ik_x x = ikz\cos\theta_2 + ikx\sin\theta_2 \tag{2.4}$$

where k is just the magnitude of the wave vector.

From Snell's Law:

$$\sin\theta_2 = \frac{n_1}{n_2}\sin\theta_1 \tag{2.5}$$

And from the identity $\cos^2\theta_2 + \sin^2\theta_2 = 1$:

$$\cos\theta_2 = \pm\sqrt{1-\sin^2\theta_2} = \pm\sqrt{1-\frac{n_1^2}{n_2^2}\sin^2\theta_1} \tag{2.6}$$

Since we are interested in the case where $\theta_1 > \theta_c$, the sine term is >1. This makes the term under the radical negative. Pulling out $i = \sqrt{-1}$ to make the radical real and positive, and rearranging:

$$\cos\theta_2 = \pm\frac{i}{n_2}\sqrt{n_1^2\sin^2\theta_1 - n_2^2} \tag{2.7}$$

Assuming the positive root (the negative root would lead to an exponentially increasing wave that is simply not realistic) and plugging the expressions for sine and cosine back into $i\vec{k}\cdot\vec{r}$:

$$i\vec{k}\cdot\vec{r} = -\frac{kz}{n_2}\sqrt{n_1^2\sin^2\theta_1 - n_2^2} + ikx\frac{n_1}{n_2}\sin\theta_1 \tag{2.8}$$

The first term will result in a decaying wave in the z-direction, while the second term will generate a propagating wave in the x-direction.

Now, what we perceive with our eyes or is detected by a camera is the *intensity* of the incident light, not the amplitude of the electric field. Intensity goes as the square of the electric field. So, ignoring the x-component:

$$I(z) = I_o \exp\left(-\frac{2kz}{n_2} \sqrt{n_1^2 \sin^2\theta_1 - n_2^2} \right) \tag{2.9}$$

From this, the penetration depth d_p can be identified as:

$$d_p = \frac{n_2}{2k} \frac{1}{\sqrt{n_1^2 \sin^2\theta_1 - n_2^2}} = \frac{\lambda_0}{4\pi \sqrt{n_1^2 \sin^2\theta_1 - n_2^2}} \tag{2.10}$$

using the conversions for the wave vector, $k = 2\pi/\lambda$, and the wavelength in the second medium relative to vacuum (or air), $\lambda_0 = \lambda n_2$. Note that the penetration depth depends upon the incident angle and wavelength of the excitation light, and the indices of refraction of the two media.

Finally, note that an intermediate layer between the two media will not affect the TIR between the two media, as long as the light can pass through the intermediate layer. For example, if there were an intermediate layer present between medium 1 and medium 2, Snell's law for each interface would be:

$$n_1 \sin\theta_1 = n_{int} \sin\theta_{int} \quad \text{and} \quad n_{int} \sin\theta_{int} = n_2 \sin\theta_2. \tag{2.11}$$

These two equations could be equated to each other, leading back to the original expression for Snell's law between mediums 1 and 2:

$$n_1 \sin\theta_1 = n_2 \sin\theta_2, \tag{2.12}$$

showing that TIR excitation is not affected by an intermediate medium.

2.3 Two Methods of TIRF Excitation

There are two basic types of TIRF microscopes. One, which I alluded to in the introduction, is to use some kind of prism to aim the excitation light at the interface

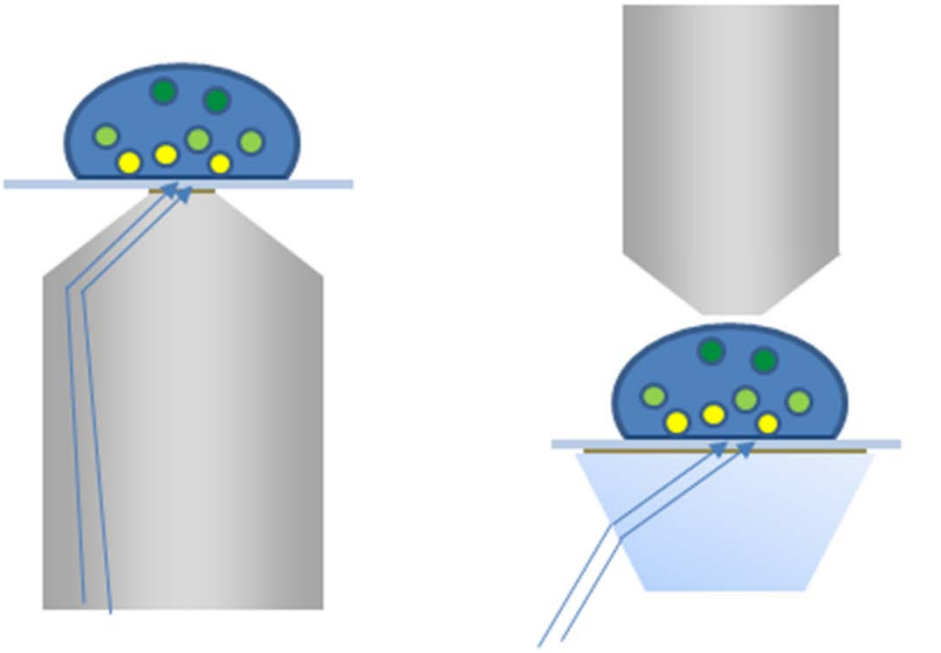

Figure 2.2. Two implementations of TIRF microscopy. Left: Objective based TIRF. Excitation light passes through the objective such that it reaches the sample at an angle greater than the critical angle. Right: TIRF with a prism. Excitation light passes through a prism to reach the sample interface at an angle greater than the critical angle.

between the coverslip and the sample of interest at an angle greater than the critical angle (Axelrod 2001b). Observation of the sample is done from the side of the sample opposite the prism (Figure 2.2, Right). As one might imagine, the ability to access or manipulate the sample is limited.

In the other, more widely used type of TIRF microscope, excitation light is applied through a high numerical aperture (NA>1.38) objective. This allows light at angles greater then the critical angle to be directed to the coverslip-sample interface through the objective (Figure 2.2, Left) (Axelrod 2001b). The same objective is used to collect the fluorescence excited in the sample. Here, since the excitation and observation are done from the same side of the sample, the other side of the sample

can be left open and accessible for manipulation of cells in the sample. Additionally, a high NA objective enables greater light gathering ability then typical objectives used in microscopy (NA ≤ 1.3). These advantages made objective-based TIRF the ideal choice for experiments I will present in later chapters.

There has been much debate over the choice of illumination source for TIRF excitation. The advantage of an arc lamp illumination source is that the excitation wavelength is limited purely by what filters are chosen. Lasers, on the other hand, have a very limited set of excitation wavelengths. Also, laser TIRF has often suffered from uneven illumination because the coherent light of a laser is prone to interference and diffraction effects. One other criticism of arc lamp TIRF systems compared to laser systems is the illumination intensity. This is not an issue I have experienced with the Annular TIRF microscope detailed below. In fact, in my experience, there is often an issue with too much excitation intensity in laser TIRF systems, resulting in the need to decrease the laser power output so as not to bleach the sample under study. To be fair, the laser excitation TIRF does have one distinct advantage over arc lamp TIRF: with the correct setup, the angle of incidence of the laser beam can be controlled very precisely. This could be useful mainly in experiments where having a very particular penetration depth could be important, such as those that involve an interpretation of data based on calculations of intensity vs. depth.

2.4 The Annular TIRF Microscope

The Annular TIRF microscope is based on an inverted Zeiss microscope (Axiovert 135 TV). The microscope was modified for TIRF microscopy by moving the microscope's arc lamp away from the rear port of the microscope to accommodate placement of excitation filters, an annular disk and a pair of achromatic doublets (spaced 3.1 mm apart, f = 300 mm, ThorLabs, Newton, NJ) into the beam path. A high

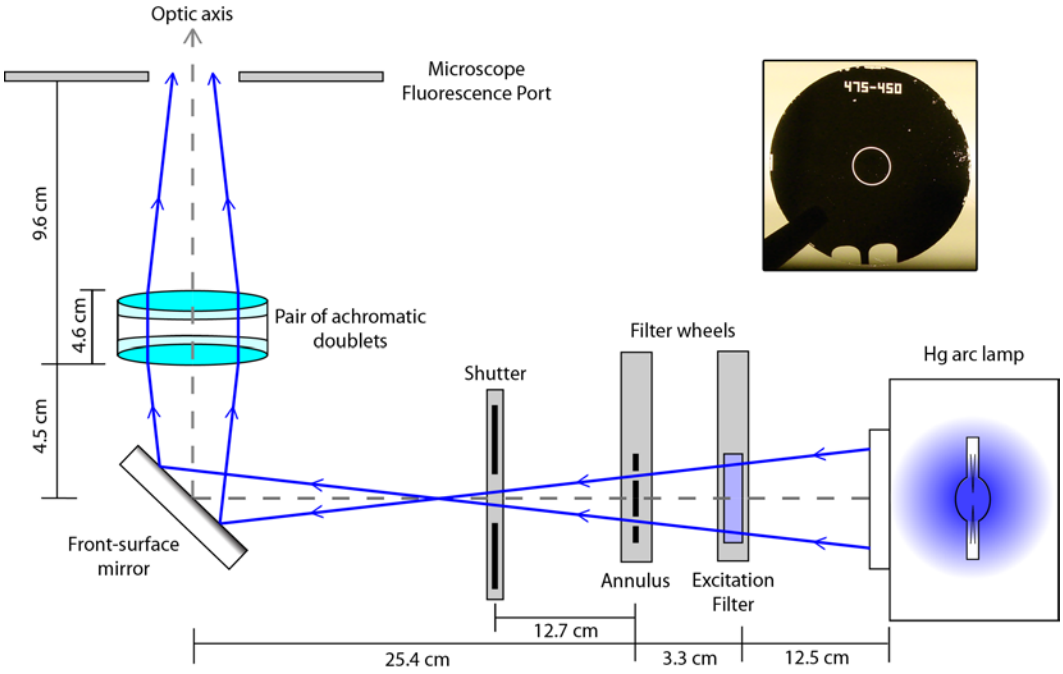

Figure 2.3. A schematic diagram showing the light path and locations of the components of the Annular TIRF microscope. The annulus was placed at the equivalent back focal plane (EBFP). Inset: an annulus used in the microscope backlit with a fluorescent bulb. The annular ring is clearly visible, with an inner diameter of 4.50 mm and outer diameter of 4.75 mm. The annulus dimensions were found as described in the text. The marks around the edge of the annulus are the result of the fabrication method and do not affect its performance.

NA objective (Zeiss plan-fluar 1.45 NA 100x oil immersion), specifically designed for TIRF microscopy, was used, and an annular disk was positioned in the equivalent back focal plane of the objective. A schematic of the modified beam path to the fluorescence port of the microscope, detailing the modifications to the microscope is shown in Figure 2.3.

The annular disk, a unique feature of this microscope, was designed such that all light would be blocked by a circle of opaque material, except for those rays that would be incident upon the sample at an angle greater than the critical angle, as was typical in early objective-based TIRF microscopes (Axelrod 2001a). Additionally, the

annulus blocks all light that may enter the microscope or objective at angles too high to pass through the objective. This reduces the amount of stray light that could be reflected or refracted inside the microscope and that could eventually make its way out through the objective at angles less than the critical angle. The result, as shown in Figure 2.3 (inset), is a device that only allows light to pass through a ring shaped aperture. The annulus was custom designed and fabricated in a clean room environment by depositing aluminum onto a glass coverslip using standard microfabrication techniques. A pair of achromatic doublets (f = 300 mm, ThorLabs, Newton, NJ) were placed between the annulus and the microscope to nullify any changes in focal length associated with different excitation wavelengths (chromatic aberration) while focusing the light into the microscope. Automated filter wheels (Lambda 10-2, Sutter Instruments, Novato, CA) and a shutter (Uniblitz VMM-T1, Vincent Associates, Rochester, NY) were added to the system to more easily and reproducibly control the placement of the annulus and excitation filters and to control the light illuminating the sample.

In addition to TIRF microscopy, this microscope still maintains its capabilities for standard epifluorescence (excitation light directed through the objective to the sample at all angles permitted by the objective) and differential interference contrast (DIC) microscopy.

2.4.1 Microscope Modification for Annular TIRF

When modifying a microscope for annular TIRF, the first task is to find an equivalent back focal plane (EBFP) to the objective's back focal plane (BFP). Ideally, an appropriately sized blocker placed at the BFP of the objective would block out all light that would reach the sample at less than the critical angle. However, the BFP is located at some unknown plane inside the objective. The solution to this problem is to instead

place a blocker at the EBFP of the objective, such that an image of the blocker is focused on the BFP. First, the "incident light fluorescence illuminator," a tube-like component of the microscope containing a lens and located in the rear fluorescence port of the microscope, was removed. To find the EBFP, the Hg arc lamp (focused "at infinity" according to the manufacturers directions) was spaced well back from the microscope fluorescence port, where it would have been mounted in a standard epifluorescence microscope. Then, following the method of Stout and Axelrod (Stout and Axelrod 1989), a razor blade was placed partway into the illumination beam between the microscope and the arc lamp and moved along the beam path until its image was in focus on a screen located above the TIRF objective. This position was marked as the EBFP.

While a single achromatic doublet would have significantly reduced the chromatic aberrations in the excitation light path, we chose to use two doublets to effectively eliminate any chromatic aberrations in the excitation light path. The effective focal length (f) of the achromatic doublet pair was approximated using the thick lens equation from Hecht (Hecht and Zajñac 1987):

$$\frac{1}{f} = \frac{1}{f_1} + \frac{1}{f_2} - \frac{d}{f_1 f_2} \tag{2.13}$$

where f_1 and f_2 are the focal lengths of the individual doublets, and d is the distance between their principle planes (d = 12.6 mm in this case). The effective focal length for the pair was found to be approximately 153 mm. The position of the achromat pair along the excitation beam path was chosen so that the magnification between the BFP and EBFP would have an approximate magnitude of one. Using another equation from Hecht (Hecht and Zajñac 1987):

$$\frac{|y_i|}{y_o} = \frac{f}{(s_o - f)} \approx 1 \tag{2.14}$$

where y_o and y_i are the transverse heights of the object and image, respectively, and s_o is the distance between the object plane (EBFP) and the principle plane of the doublet pair. From relation 2.14, $s_o = 2f \approx 306$ mm. Therefore the doublets were placed approximately 30.6 cm down beam (towards the microscope) from the EBFP.

The dimensions for the annular blocker were found by passing light from the arc lamp through a pinhole mounted on a caliper and placed at the EBFP. A hemispherical lens was placed atop the objective to allow light at angles greater than the critical angle to be observed. A cylindrical screen, marked with the critical angle between a cell and coverslip, was placed concentric to the hemispherical lens (Figure 2.4). The pinhole was moved until its image on the screen fell upon the cylindrical screen at the critical angle, and its caliper position noted. The pinhole was then moved to the critical angle mark on the opposite side of the cylinder and its position noted on the caliper in order to determine the minimum inner diameter of the annulus. The outer diameter was determined similarly.

Typically, a focusing optic is present between the illumination source and the EBFP (see for example Stout and Axelrod 1989). In this microscope, the arc lamp itself performs this duty. Initially, the arc lamp is focused “at infinity” per the manufacturer’s directions. After the lamp is placed in the TIRF microscope setup, its focus is adjusted to give the best illumination of the annular ring with a minimum of background light when viewed with the hemisphere lens and cylindrical screen described above and shown in Figure 2.4. The ideal focus varies somewhat from arc lamp bulb to bulb.

When the microscope modifications were made, the annulus and achromatic doublets were put on xyz stages to allow for position adjustments to fine-tune the system. The shutter and excitation filter wheel were placed where there was adequate space and would not disturb the beam path of the essential TIRF components.

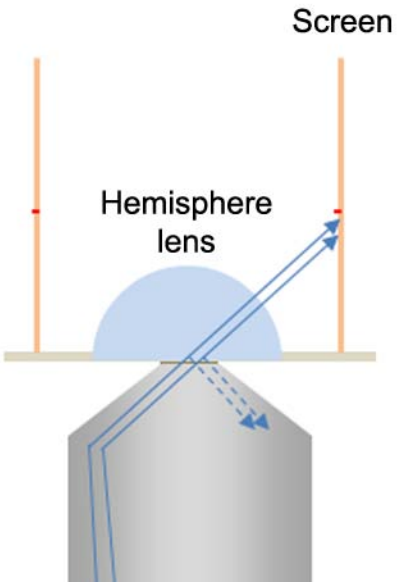

Figure 2.4. A hemispherical lens placed atop the TIRF objective allows light greater than the critical angle to be viewed on a clyndrical screen concentric to the lens. Dashed arrows indicate a path the light could have taken if a flat coverslip were put in place of the lens. Red marks on the screen indicate where light passing through the objective at the critical angle would fall.

Additionally, the excitation filters were placed as close to the arc lamp as possible in order to minimize any undesirable polychromatic reflected or refracted light further down the beam path, and increase user eye safety.

2.4.2 Annular TIRF Microscope Depth of Illumination

The calculated penetration depth for this microscope, using the equation 2.10 and excitation wavelengths based on a 480/40 nm excitation filter (Chroma Technology, Rockingham, VT) gives a possible range of depths from 81-123 nm for a standard coverslip (n=1.518)/cell (n~1.38) interface. Experimental measurement of the penetration depth is nontrivial. There have been a variety of schemes introduced over

the years in attempt to ascertain the penetration depth of TIRF microscopes experimentally. A method developed recently by Mattheyses and Axelrod (Mattheyses and Axelrod 2006), provides a fairly simple method to calculate the experimental penetration depth. Briefly, 5.08 μm diameter silica microspheres ($n \approx 1.42$; Bangs Laboratories) were coated with fluorescent DiI-C_{18}-3 (Molecular Probes/Invitrogen, Carlsbad, CA) and placed in an index matching water-glycerol solution ($n \approx 1.42$), to reduce any scattering from the spheres. A droplet of the bead solution was placed on a coverslip and the beads were allowed to settle to the coverslip surface. The beads were then imaged with the objective focused at the coverslip interface. Knowing that the center of the image of each microsphere will be the point where the microsphere is in contact with the coverslip, the microsphere radius, and using the concept that the evanescent wave will excite fewer fluorophores on the portions of the microspheres further from the surface, one can calculate the fluorescence intensity of the microspheres as a function of depth. Exponentials fit to the resulting intensity vs. depth measurements will yield an experimental value for the penetration depth of the microscope.

These calculations gave experimentally measured penetration depths for this microscope, measured with the assistance of nine groups of students in the Biophysical Methods Advanced Lab course, between 63 and 202 nm, with an average depth of 123 nm. However, the index of refraction of a cell is lower then the water-glycerol mixture, which means for the same angle of incidence, the penetration depth into a cell will be somewhat smaller then for the water-glycerol solution.

Rearranging equation 2.10:

$$n_1^2 \sin^2 \theta_1 = \left(\frac{\lambda_0}{4\pi d_p} \right)^2 + n_2^2 \tag{2.15}$$

and using the water-glycerol index and penetration depth, one can back out an "effective θ_1" that can then be used to estimate the penetration depth in a different medium atop the coverslip. Using the average coverslip/water-glycerol d_p to calculate the effective θ_1 from equation 16, the estimated penetration depth for a coverslip/cell interface is 82-85 nm, in good agreement with the calculated range.

2.5 Conclusions

The Annular TIRF microscope has become a highly useful tool for the study of exocytotic phenomena. In many of the experiments performed with this microscope, it functions in tandem with planar microelectrodes, adding a new layer of versatility. In chapter three, it was used in epifluorescence mode (prior to the TIRF conversion), and in chapters four, five, and six, observations were made in TIRF mode.

2.6 Acknowledgements

I thank Andrew Dias, who did some of the initial calculations and assisted in the modification of the microscope, and Ismail Hafez for assistance with additional modifications to the microscope. I also thank Manfred Lindau for the opportunity to present lectures on TIRF microscopy in his Biophysical Methods course, and to design and teach the TIRF microscopy portion of the Biophysical Methods Advanced Laboratory course. These experiences became the inspiration and foundation of this chapter. I also thank the students in the Advanced Laboratory course, who over the years collected penetration depth data for the Annular TIRF microscope.

REFERENCES

Axelrod, D. (1981). "Cell-substrate contacts illuminated by total internal reflection fluorescence." Journal of Cell Biology **89**(1): 141-5.

Axelrod, D. (2001a). "Selective imaging of surface fluorescence with very high aperture microscope objectives." J Biomed Opt **6**(1): 6-13.

Axelrod, D. (2001b). "Total internal reflection fluorescence microscopy in cell biology." Traffic **2**(11): 764-74.

Born, M. and E. Wolf (1970). Principles of optics; electromagnetic theory of propagation, interference and diffraction of light. Oxford, New York,, Pergamon Press.

Fornel, F. d. r. d. (2001). Evanescent waves : from Newtonian optics to atomic optics. New York, Springer.

Hecht, E. and A. Zajñac (1987). Optics. Reading, Mass., Addison-Wesley.

Mattheyses, A. L. and D. Axelrod (2006). "Direct measurement of the evanescent field profile produced by objective-based total internal reflection fluorescence." J Biomed Opt **11**(1): 014006.

Mirabella, F. M., Ed. (1993). Internal reflection spectroscopy : theory and applications. Practical spectroscopy series. New York, Marcel Dekker.

Newton, I. (1952). Opticks; or, A treatise of the reflections, refractions, inflections & colours of light. Based on the 4th ed., London, 1730. New York,, Dover Publications.

Oheim, M. (2001). "Imaging transmitter release. II. A practical guide to evanescent-wave imaging." Lasers Med Sci **16**(3): 159-70.

Stout, A. L. and D. Axelrod (1989). "Evanescent Field Excitation of Fluorescence by Epi-Illumination Microscopy." Applied Optics **28**(24): 5237-5242.

CHAPTER 3

ELECTROCHEMICAL AND FLUORESCENCE IMAGING OF FUSION PORE OPENINGS USING ELECTROCHEMICAL DETECTOR (ECD) ARRAYS[*]

3.1 Abstract

Opening of individual exocytotic fusion pores in chromaffin cells was imaged electrochemically with high time resolution. Electrochemical detector (ECD) arrays that consist of 4 platinum (Pt) microelectrodes were microfabricated on a glass coverslip. Exocytosis of single vesicles containing catecholamines from a cell positioned on top of the array is detected by the individual electrodes as a time-resolved oxidation current, reflecting the time course of arrival of catecholamine molecules at the electrode surfaces. The signals exhibit low noise and reveal foot signals indicating fusion pore formation and expansion. The position of individual release events is determined from the fraction of catecholamines recorded by the individual electrodes. Simultaneous fluorescence imaging of release of acridine orange from individual vesicles confirmed the electrochemical position assignments. This electrochemical camera provides very high time resolution, spatio-temporal localization of individual fusion pore openings and quantitative data on the flux of transmitter from individual vesicles. Analysis of the amperometric currents employing random walk simulations indicates that the time course of amperometric spikes measured near the cell surface is due to a low apparent diffusion coefficient of catecholamines near the cell surface and not due to slow dissociation from the granular matrix.

[*] The majority of this chapter appears as "Electrochemical imaging of fusion pore openings by electrochemical detector arrays" by I. Hafez, K. Kisler, K. Berberian, G. Dernick, V. Valero, M.G. Yong, H.G. Craighead, and M. Lindau in *Proceedings of the National Academy of Sciences of the United States of America* 102:13879-13884 (2005).

3.2 Introduction

Exocytosis (Almers 1990) is responsible for release of neurotransmitters, peptides, hormones and various mediators of the immune system. During exocytosis the molecules stored within membrane bound secretory vesicles inside the cell are released by fusion of the vesicle membrane with the cell's plasma membrane. A critical event that attracted much attention is the formation and expansion of the fusion pore (reviewed in (Lindau and Alvarez de Toledo 2003)) through which the vesicular cargo molecules are released.

Chromaffin cells from the adrenal gland are a widely used model system to study neuronal exocytosis and the fusion pore properties in these cells have been studied in great detail (Albillos, Dernick et al. 1997; Alés, Tabares et al. 1999; Tabares, Ales et al. 2001; Dernick, Alvarez de Toledo et al. 2003). Release of single vesicles (quanta) of epinephrine or norepinephrine (adrenaline or noradrenaline, respectively) can be detected electrochemically with a carbon fiber electrode (CFE) as amperometric spikes *(Wightman, Jankowski et al. 1991; Chow, Rüden et al. 1992).* These spikes are often preceded by a so-called foot signal (Chow, Rüden et al. 1992), which is due to slow discharge of catecholamines through a narrow fusion pore (Albillos, Dernick et al. 1997) and indicates the time of fusion pore formation and expansion.

To obtain not only temporal but also spatial resolution of opening and expansion of single fusion pores in chromaffin cells, we fabricated electrochemical detector (ECD) arrays of four Pt electrodes patterned on glass coverslips (Dias, Dernick et al. 2002). For quantal events, the oxidation currents recorded from the four electrodes allow the desired determination of fusion pore dynamics with millisecond time resolution as well as localization of the fusion event. Simultaneous observation of the cell by fluorescence microscopy can be performed. Here we show that the spatio-

temporal assignments of single exocytotic events obtained by electrochemical imaging of fusion events correlates with release of a fluorescent vesicle marker during exocytosis in chromaffin cells.

3.3 Materials and Methods

3.3.1 Electrochemical Detector Array

Pt conductors insulated by photoresist were fabricated photolithographically on standard microscope coverslips No. 1.5 (160-190 µm thick) as described (Dias, Dernick et al. 2002) forming a 4-electrode ECD array. Each ECD array consists of a square window approximately 10 x 10 μm^2 in size in the insulating 0.5 µm thick photoresist. The active electrodes are formed by the tips of the four Pt conductors, approximately 3 µm wide and 150 nm thick that protrude into the corners of the square. The area and shape of the electrode arrays were imaged and quantified using atomic force microscopy and optical microscopy.

3.3.2 Cell Preparation and Recording Conditions

Bovine adrenal glands were obtained from a local slaughterhouse and prepared as described (Parsons, Coorssen et al. 1995). Cells were cultured on 12 mm coverslips that were coated with 0.02% poly-D-lysine and used on days 1-10. Before the experiment, a small coverslip with cells attached was placed in a 35 mm dish containing 1 mL of bath solution containing (in mM): 150 NaCl, 10 HEPES, 5 $CaCl_2$, 5 KCl, 2 $MgCl_2$, pH =7.25 (318 mOsm) and supplemented with 3 µM acridine orange (Molecular Probes, Eugene, OR) for 15 minutes in the dark. An ECD array coverslip was mounted on a custom-built stage on a Zeiss Axiovert 135TV microscope and the coverslip with the cells was placed at some distance from the ECD array. 150-200 µL of bath solution was then added to cover the cells and the active electrode array. Using

a patch pipette, a cell was lifted off the coverslip and manipulated over the center of an ECD array. Some cells were stimulated by including ionomycin in the pipette or adding ionomycin to the bath. Experiments were performed at room temperature.

3.3.3 Electrochemical Recording and Analysis

The ECD electrodes were connected via their contact pads to four current amplifiers operating on a single power supply with a four-channel head stage (VA-10, NPI Electronic, Tamm, Germany) and the built-in filters set to 500 Hz. The amperometric currents were simultaneously recorded using a holding potential of +700 mV relative to a common Ag/AgCl electrode immersed into the bath and sampled at 1 kHz. Amperometric current spikes were subjected to a rolling integration in order to obtain the fraction of charge detected at each electrode. Position assignments from amperometric data were obtained as described in the *Results* section. For graphical display only, current traces were further smoothed using a binomial algorithm using IGOR Pro (Wavemetrics, Lake Oswego, OR).

3.3.4 Random Walk Simulations and Deconvolution Fits

Random walk simulations were programmed using the Java programming language and Forte for Java CE 3.0 (Sun Microsystems, Santa Clara, CA) as described in the *Results* section and the position of measured events determined by least squares fitting to give best agreement between measured and simulated fractional charges for each of the four electrodes. For time course analysis of a given event random walk simulations were performed for its location using 2,000,000 molecules to obtain a low noise time course for the simulated signals of the four electrodes. The experimental ECD signals and simulated signals were integrated using IGOR Pro. Because the data was sampled at 1 ms/point, the release time course was approximated by a series of instantaneous

release events of different amplitudes, each occurring every 1 ms. At each time point t_i, the release amplitude $r(t_i)$ was fit to the experimental time course $D(t_i)$, using the random walk diffusion signals ($D_{RW}(t)$). These amplitudes were fit using the equation:

$$D(t_i) = \sum_{j=0}^{i} r(t_j) \cdot D(t_i - t_j)$$

employing procedures written in IGOR Pro. The release amplitudes were fit globally such that convolution with the four integrated random walk diffusion functions gave best agreement with the four integrated experimental signals. Fits were performed for various diffusion constants until the best fit was obtained for each secretory event.

3.3.5 Fluorescence Imaging

During the experiment the bottom of the cell was imaged using a 100 x 1.30 NA Fluar oil-immersion objective and low-fluorescence immersion oil (Immersol 518 F, Zeiss, Germany) with a cooled, 12-bit CCD camera (Quantix 57; Photometrics, Tuscon, AZ) mounted to the bottom port of the microscope. Images were 2x2 binned and the exposure for each image was 100 ms with a 9 ms inter-exposure period. At these settings the image pixel size was 260 nm. For synchronization image exposure times the exposing output of the Quantix 57 was recorded in a separate channel on a 16-bit A/D converter together with the four amperometric currents. Epi-illumination was from a 75 W Xenon arc lamp attenuated using a neutral density filter of optical density 3.0 and a 480/40 nm excitation filter, 505 nm LP dichroic, and a 535/50 nm emission filter (Omega Optical, Inc. and Chroma Technology, both of Brattleboro, VT).

3.3.6 Image Analysis

Images were acquired and processed using V++ software and its built-in routines (Digital Optics, New Zealand). Single frames (n) from acquired sequences were extracted as signed 32-bit images. To recognize dequenching "flashes" occurring upon exocytosis of a vesicle, a rolling subtraction procedure was implemented providing difference images according to the following scheme: For a sequence of 6 images ($IMAGE_n$....$IMAGE_{n+5}$), difference images ($DIFFERENCE_i = IMAGE_i - AVERAGE$, i = n...n + 5) were generated by subtracting the average of 10 images preceding the first image in the sequence ($AVERAGE = \sum_{j=1}^{10} IMAGE_{n-j}/10$). The 32-bit difference images contained both negative and positive values. The difference images of the sequence (n…n+5), were scaled and converted to 8-bit gray scale images such that the minimum and maximum pixel values found in the sequence were converted to values of 0 and 255, respectively. Difference sequences that contained clear indications of a sudden intensity increase (flashes) were manually selected and automatically logged

3.4 Results

3.4.1 ECD Recordings

For a typical experiment a chromaffin cell was picked up by a patch pipette sealed onto its surface using standard methods (Hamill, Marty et al. 1981). Using the pipette, the cell was manipulated over an ECD array of four amperometric Pt electrodes and mechanically pushed gently onto the surface as indicated by the bottom of the cell being in the same focal plane as the electrodes (Figure 3.1A). In the presence of calcium amperometric spikes indicating individual exocytotic events were recorded from all four electrodes in response to the mechanical stimulation (Figure 3.1B). One of these events is shown on an expanded time scale in Figure 3.2A. For this event, the

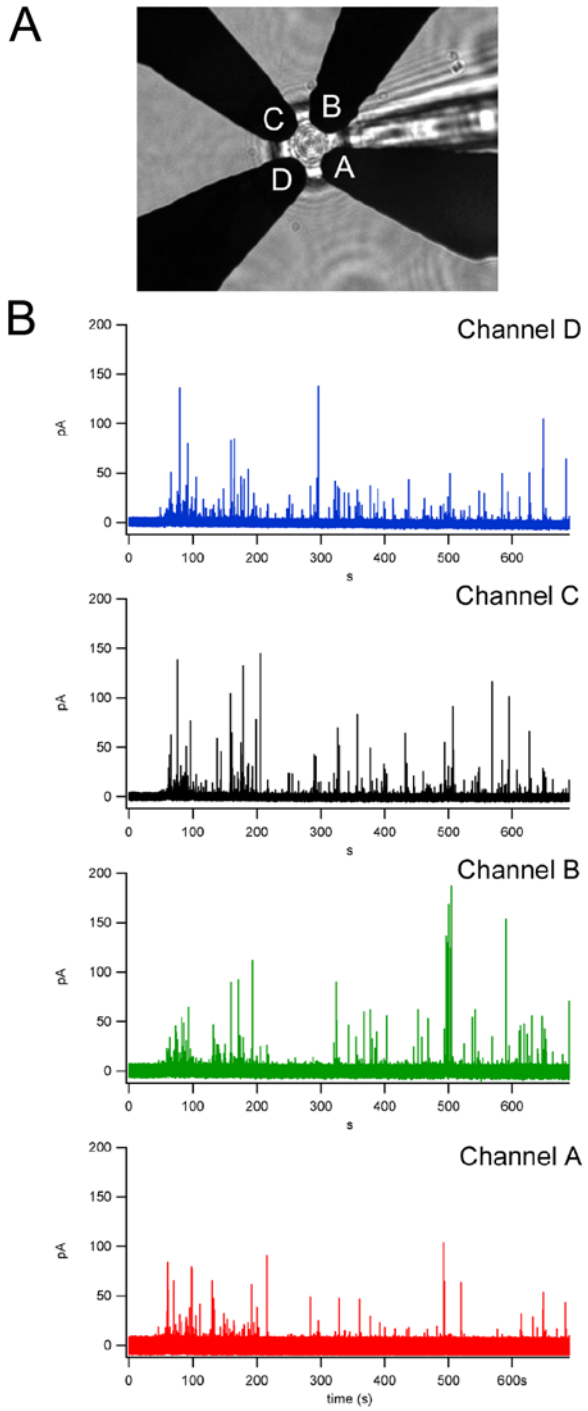

Figure 3.1. (A) Light microscope image of a chromaffin cell placed on top of an ECD array, with four electrodes labeled A through D. (B) Amperometric recordings from the four electrodes (Channel A red, B green, C black, D blue trace) recorded from a single bovine chromaffin cell mechanically stimulated by a patch pipette in calcium containing external solution.

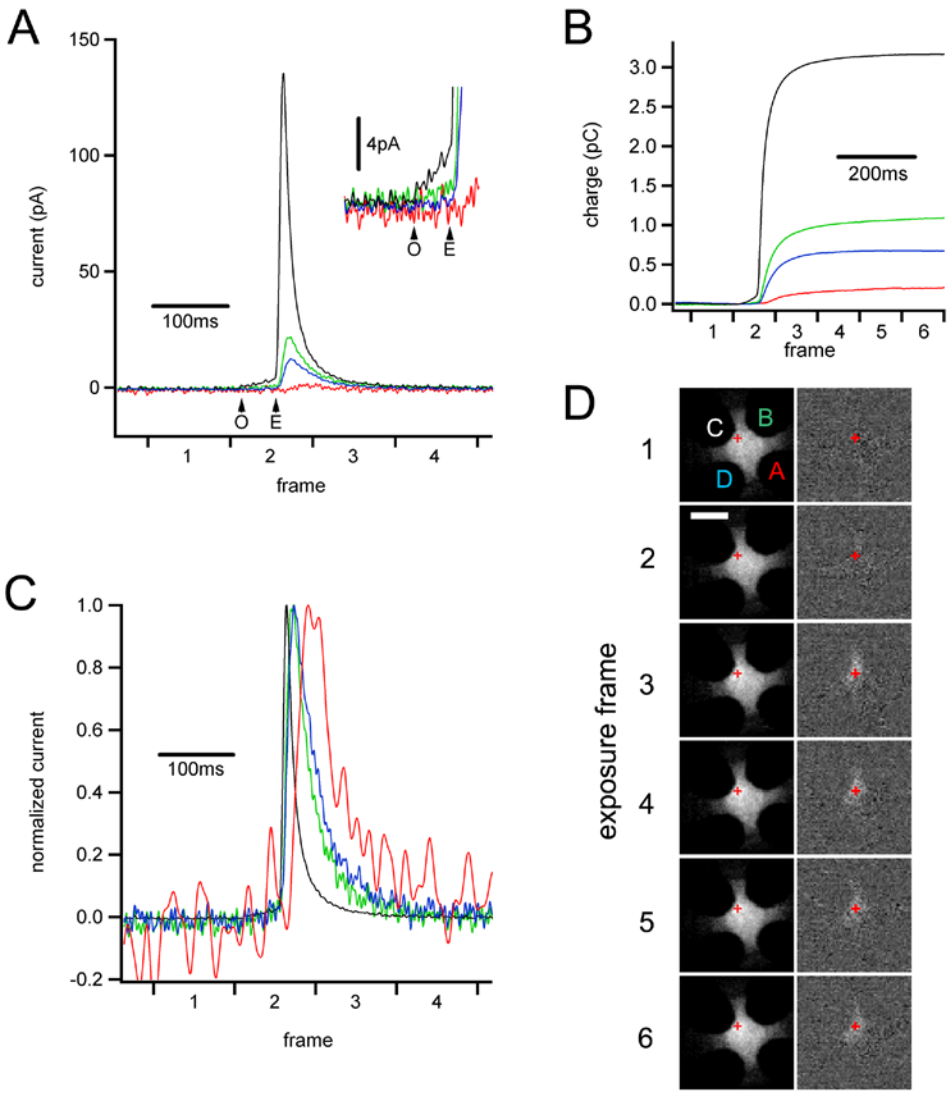

Figure 3.2. (A) One exocytotic event from the experiment of Figure 3.1 shown on an expanded time scale. Arrows mark start and end of the foot signal (black trace) indicating fusion pore opening (O) and expansion (E), respectively. The foot signal is shown on expanded current scale in the inset. (B) Running integrals of the amperometric currents provide the total charge detected by the individual electrodes. (C) Currents from the four electrodes after normalization of the amplitudes reveal differences in time course for the different signals. (D) Spatio-temporal correlation of secretion of catecholamines and release of the fluorescent vesicle marker acridine orange. (Left) Original sequence of fluorescence images. (Right) Difference images obtained by subtracting the average of 10 images preceding the sequence. The exposure times for each frame are indicated on the horizontal axes of panels A-C. The fluorescence "flash" in the difference images indicates the position of the exocytotic event. The release position calculated from the electrochemical signals (B) is indicated in (D) as a red cross (scale bar 5 µm)

signal from electrode C is largest followed by that of electrode B and electrode D. The signal from electrode A is just detectable. In this cell 57 out of 211 events showed a detectable amperometric spike in 3 or 4 electrodes. The remaining events showed amperometric spikes in only 1 or 2 electrodes. In a second mechanically stimulated cell 14 out of 27 events showed amperometric spikes in 3 or 4 electrodes. In ionomycin stimulated cells < 5% of events showed amperomtric spikes in 3 or 4 electrodes.

As with CFEs, a foot signal preceding the spike of catecholamine release is clearly visible in the large signal recorded by electrode C indicating formation and expansion of the fusion pore (arrows in Figure 3.2A). The duration of this foot signal was 48ms. In this cell 87 out of 211 events showed a detectable foot signal. The mean duration of these foot signals was 18ms. In a second cell 22 out of 27 events showed a detectable foot signal with a mean duration of 22 ms. The average integrated charge of the foot signals was 51 fC and 70 fC in the two cells, respectively. In 2 cells stimulated with the calcium ionophore ionomycin 40% of the events showed foot signals with mean durations of 12 ms and 15 ms, and mean foot charges of 34 fC and 73 fC. The properties of foot signals observed with ECD arrays are thus similar to those reported for CFE amperometry of chromaffin cells (Chow, Rüden et al. 1992; Zhou, Misler et al. 1996).

Figure 3.2B shows the running integrals of the four currents indicating the charge measured by each electrode. The current signals provide a low noise measure of catecholamine release and again clearly indicate the foot signal. The total amperometric charge for this event (sum of the four partial charges) was 5.3 pC corresponding to 1.7×10^7 catecholamine molecules. The mean total charge of all events from this cell was 2.0±1.5 pC (SD, n=211). The mean charge of single events in a second mechanically stimulated cell was 1.5±1.4 pC (SD, n=27). Mean charge in

2 ionomycin-stimulated cells was 1.3±1.9 pC (SD, n=160) and 0.63±0.36 pC (SD, n=143). The quantal size of events recorded by ECD arrays is thus in the same range as that of events recorded with CFEs (Wightman, Jankowski et al. 1991; Wightman, Schroeder et al. 1995; Zhou, Misler et al. 1996; Albillos, Dernick et al. 1997).

3.4.2 ECD Imaging

Assuming that free diffusion of released molecules in the space between the cell surface and the surface of the coverslip between the ECD electrodes is equally possible in all directions, and that each electrode effectively oxidizes all molecules arriving at its surface, we expect the individual release event to be located closest to the electrode detecting the largest fraction of charge. Based on this assumption we would locate the event depicted in Figure 3.2 to be closest to electrode C and far from electrode A. Figure 3.2C shows the four amperometric signals superimposed after normalization to the same amplitude. The signals are slower the smaller they are, consistent with longer diffusion times to the more distant electrodes.

To determine quantitatively the position of release from the fractional charges measured by the four electrodes, random walk simulations were performed to estimate the fraction of molecules arriving at the different electrodes, depending on the position where vesicle contents were released. The positions and shapes of the detectors used in a particular experiment were determined by atomic force microscopy and optical microscopy from which a matrix was created in the computer reflecting the actual electrode geometries (Figure 3.3A). The cell was modeled as a semi-infinite cylinder with a flat 10 μm diameter bottom surface suspended 100 nm above the Pt electrode surfaces. Release sites were set up in a 0.5 μm grid on this surface. Release from individual sites was assumed to be instantaneous and diffusion was modeled by

Figure 3.3. (A) Outline of the detector map (red lines) used for the random walk simulations overlayed on image of the actual electrodes. The dashed blue circle indicates the central area with 2 μm radius. (B) Difference images (a-v) of all 22 fluorescence flashes from this cell for which position assignments were obtained. The red crosses (at end of arrows) indicate the position assignments from electrochemical imaging. Difference image (i) shows the event of Figure 3.2. In all cases the fluorescence flash appeared in the image frame immediately following the spike of catecholamine release measured electrochemically. (C) Comparison of the measured x-coordinates obtained from electrochemical and fluorescence imaging. (D) Comparison of y-coordinates. The dashed lines with slope 1 would be expected for perfect agreement between the two independent measurements. The red data points refer to events located outside the blue circle of Figure 3.3A.

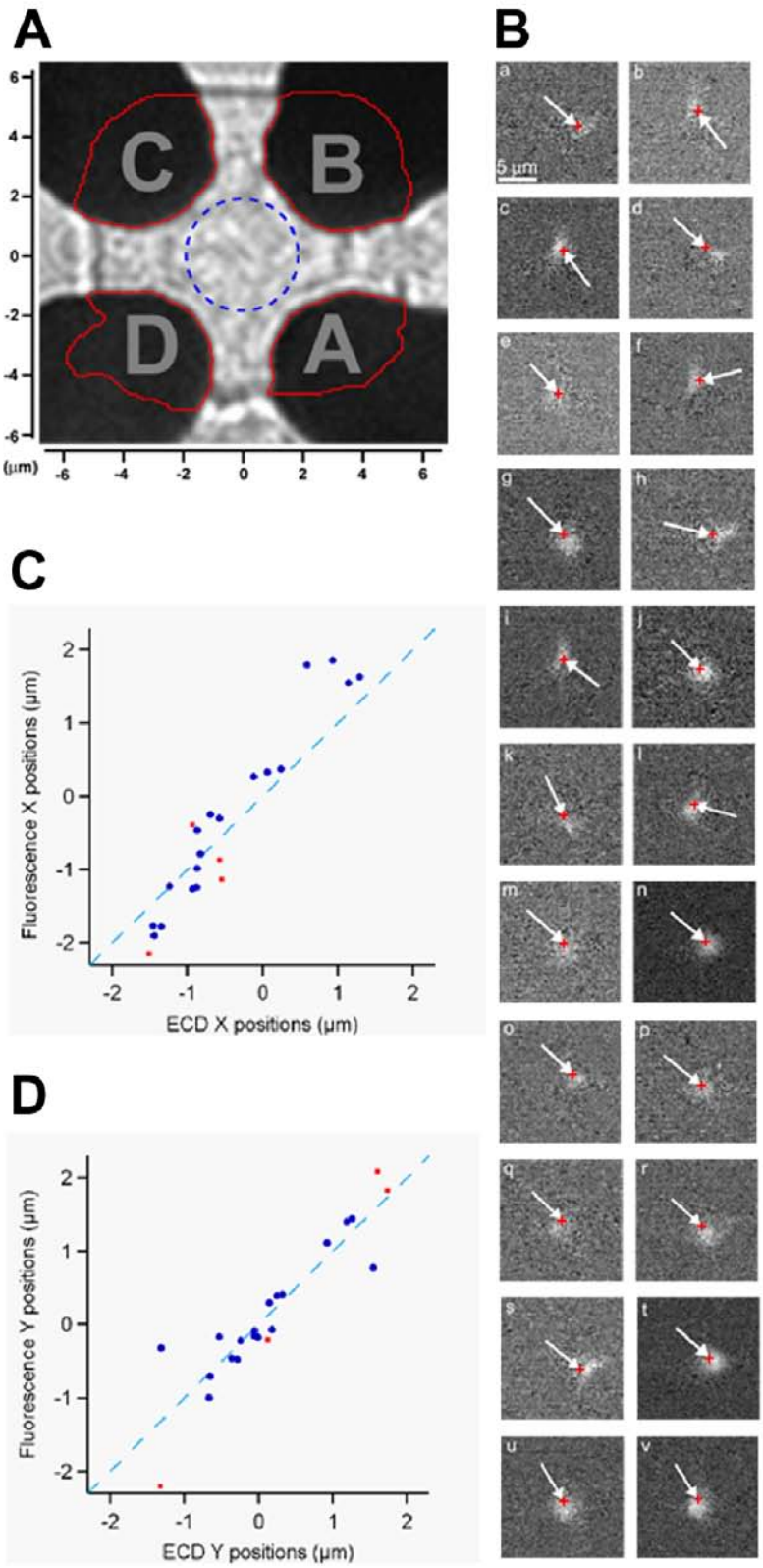
A
C
B
D
A
(µm)
B
5 µm
C
Fluorescence X positions (µm)
ECD X positions (µm)
D
Fluorescence Y positions (µm)
ECD Y positions (µm)

random walk simulations for 10,000 molecules per vesicle. These fractional charges depend only on the locations of the particular release sites and on the geometries of the different electrodes. They depend neither on the particular diffusion coefficient assumed in the simulation nor on the particular time course of release. The position of the measured events was fit to give best agreement between measured and simulated fractional charges for each of the four electrodes using interpolation between the release sites chosen in the random walk simulations.

We have chosen to model the cell by a semi-infinite cylinder rather than a disk to approximate the cell geometry encountered by molecules diffusing out of the 10 μm disc area. Although some molecules released from the bottom surface escape detection in the simulation, the estimated fraction of "lost" molecules from simulated exocytotic events was always very small (< 1%). As expected, many release events are recorded in only 1 or 2 channels. For events that appeared in traces from two electrodes, these electrodes were always adjacent to each other as expected for events at the ECD periphery. However, neither can we assign a position to events that appear in only 1 or 2 electrodes, nor is the fluorescence dequenching flash likely to be observed. Thus, these events were not included in the analysis performed here. Release events that do not occur near the bottom surface produce amperometric signals with very small amplitude and very slow time course. Such signals were never observed in more than 2 electrodes.

3.4.3 Comparison with Fluorescence Imaging

To independently confirm the positions obtained with electrochemical imaging, we simultaneously performed fluorescence imaging on the same cell. The secretory vesicles were loaded with acridine orange, a dye that accumulates in acidic compartments at high concentrations such that its green fluorescence is partially

quenched and red-shifted (Williams and Webb 2000). Upon exocytosis the dye is diluted which manifests itself by a dequenching flash of green fluorescence (Steyer and Almers 1999; Avery, Ellis et al. 2000). Figure 3.2D (left) shows a sequence of six fluorescence images. The average of 10 images preceding this sequence was subtracted from each individual image in the sequence providing the difference images (Figure 3.2D, left). The dequenching flash in the difference images is correlated with the time course of catecholamine secretion (Figure 3.2B). The position of this event obtained from electrochemical imaging (Figure 3.2D, red cross) matches the position of the dequenching flash.

The 22 fluorescence dequenching flashes (Figure 3.3D) from difference images obtained as in Figure 3.2D agree well with the corresponding ECD position assignments (red crosses at arrow tips). For a quantitative comparison, we assigned a position to each fluorescence dequenching flash (Figure 3.3B) as the center of the brightest 4 pixels in the difference image. For most events determining center of mass gave essentially the same result. However, for events that had a flash that was partly covered by one of the electrodes, the center of mass approach was less suitable. To analyze all events in a consistent way we have thus chosen to use the 4 brightest pixels to determine the position. A coordinate system was chosen according to the symmetry of the ECD array as shown in Figure 3.3A. Figure 3.3C and Figure 3.3D show the comparison between the x and y positions obtained by electrochemical array imaging and the positions of the corresponding fluorescence dequenching flashes. The dashed lines indicate a slope of 1 as expected for perfect agreement between electrochemical imaging and fluorescence imaging. The data points are close to these lines.

The mean absolute deviation between the coordinates obtained from electrochemical and fluorescence imaging in this cell was 410 nm for the x-direction and 280 nm for the y-direction (n=22). Since the precision of electrochemical imaging

is better in the central area between the electrodes, analysis using only data points lying within 2 μm from the center (Figure 3.3A, circle) gave smaller mean deviations (330 nm for x-direction and 190 nm for y-direction, n=18). It should be noted that the fluorescence dequenching flashes are very diffuse and the assignment of its position is not very precise. The values obtained for the accuracy of the ECD should thus be considered upper limits of the error of electrochemical imaging.

3.4.4 Kinetic Analysis

For comparison with CFE recordings we analyzed the width of the amperometric spikes at half maximum ($t_{1/2}$) for the largest signal of each event, which is obtained from the electrode closest to the release site. The mean $t_{1/2}$ values were 19.5±14.4 ms (SD, n=211) and 9.2±2.7 ms (SD, n=27) for the mechanically stimulated cells and 15.1±22.6 ms (SD, n=160) and 12.1±8.3 ms (SD, n=143) for the ionomycin-stimulated cells. These values agree well with those obtained with conventional CFE recordings with cell-electrode distances of 1 μm or less (Wightman, Schroeder et al. 1995).

The random walk simulations for various release positions provide not only the fractional charges but also a time courses of the amperometric signals. Assuming that quantal release is instantaneous and using the standard diffusion constant $D = 6x10^{-6}$ cm^2/s for epinephrine (Gerhardt and Adams 1982), the simulated random walk signals were always faster than the measured signals (data not shown). This is not unexpected (Wightman, Schroeder et al. 1995) since the measured signals are in fact a convolution of the release kinetics with the appropriate diffusion function. Using the diffusion functions determined by the random walk simulations, we thus performed a deconvolution to determine the underlying release kinetics (Figure 3.4A) by least squares fitting of the release function to the running integrals of the measured

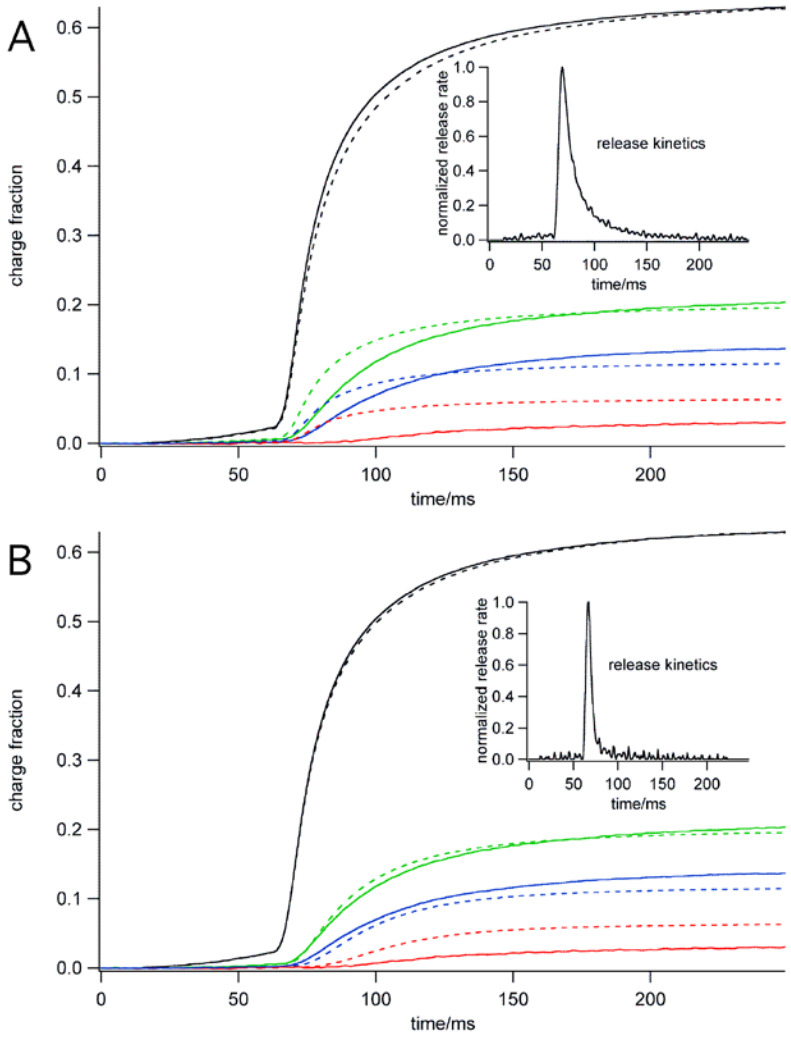

Figure 3.4. Integrated experimental (solid lines) and fitted (dashed lines) amperometric signals using (A) the standard diffusion constant D = 6 x10^{-6} cm^2/s and (B) a diffusion constant of D = 8 x10^{-7} cm^2/s. Insets show the time course of release resulting from the fits. All four traces were fitted simultaneously.

amperometric signals (see *Materials and Methods*). While the largest signal is rather well reproduced by the fit, the smaller signals are not fitted well. For the small signals the measured time course is significantly slower than the simulated time course (Figure 3.4A). Since the electrodes measuring smaller signals are further away from

the release site, this result suggested that diffusion is in fact slower than assumed in the simulation. We thus varied the diffusion coefficient assumed for determining the diffusion function and repeated the deconvolution fits. Diffusion constants up to 30 times lower than the value for free diffusion were tested. The best agreement was obtained using a diffusion coefficient $D = 8 \times 10^{-7}$ cm^2/s (Figure 3.4B). For 7 events from 2 different cells the best fits were obtained with diffusion coefficients in a narrow range between 8×10^{-7} cm^2/s and 13×10^{-7} cm^2/s. Thus the apparent diffusion coefficient near the cell surface is about 10 times slower than for free diffusion.

3.5 Discussion

Pt ECD arrays appropriate for cellular dimensions can be fabricated directly on glass coverslips (Dias, Dernick et al. 2002). Patterned Pt microelectrodes are thus suitable to perform amperometric measurements of single exocytotic events by oxidation of the catecholamines released from individual vesicles. Mechanical stimulation of chromaffin cells manipulated over the ECD array evokes exocytotic events that generate low noise amperometric signals at the different electrodes. Mechanically stimulated release has been shown to be calcium-dependent (Wightman, Jankowski et al. 1991; Albillos, Dernick et al. 1997; Dernick, Alvarez de Toledo et al. 2003) and thus presumably involves the same neuronal SNARE-mediated fusion mechanism as release that is stimulated by receptor agonists, K^+ depolarization or calcium influx into permeabilized cells. The properties of single events recorded with the Pt ECD arrays are indistinguishable from those reported for previous CFE amperometry with respect to quantal size, spike half width, and foot duration. It can thus be concluded the recorded events resemble those induced by physiological stimulation.

3.5.1 Electrochemical Imaging

Events that produce amperometric spikes in 3 or 4 electrodes occur in the central area between the electrodes. About 30% of events from mechanically stimulated cells occurred in this area and analysis of the fractions of molecules detected by the different electrodes allows for spatio-temporal localization of individual fusion pore openings on the cell surface. The ECD array thus acts as an electrochemical imaging device with millisecond time resolution.

By simultaneous fluorescence imaging we showed directly that secretion of the fluorescent vesicle marker acridine orange occurs in concert with the secretion of catecholamine from the same vesicle. The observed fluorescence cloud decays much more slowly than the amperometric current. This is expected since the catecholamine molecules are rapidly consumed during the oxidation process, whereas the fluorescent molecules are diluted slowly in the diffusion process. A similarly slow decay is observed when catecholamines are measured with cyclic voltammetry, a method which reversibly oxidizes and reduces the molecules without the consumption of molecules that occurs in constant voltage amperometry (Wightman, Schroeder et al. 1995).

The spatial precision was estimated by comparing positions obtained by electrochemical imaging with positions obtained by fluorescence imaging. The mean distance between positions obtained with the two methods was 510 nm. However, the fluorescence dequenching flashes are very diffuse and the assigned position is thus not very precise and the distance of 510 nm is presumably an overestimate. For events within the 4μm diameter central circle, the mean absolute deviation between the coordinates from fluorescence imaging and from electrochemical imaging was 330 nm for the x-direction and 190 nm for the y-direction. The deviation is somewhat larger for events outside that area. While the agreement is very good for the y-direction

(Figure 3.3D), fitting the points for the x-direction (Figure 3.3C) gave a slope of 1.37±0.08, suggesting that a small systematic error exists. Such errors may result from small errors in the boundaries of the electrodes or from some debris near the boundaries of the electrodes. However, the mean deviations are rather small and comparable to the point-spread-function of the microscope.

Proper localization of fusion pore openings requires that all electrodes of the array are equally sensitive catecholamine detectors. The good correspondence between electrochemical and fluorescence imaging indicates that this is the case but how can this be ensured independent of fluorescence imaging. An important criterion for a "good" sensitive amperometric electrode is that it rapidly oxidizes catecholamine molecules. indicated by brief amperometric spikes with short half width. Release events from chromaffin cells typically have a half-width of 10-20 ms when recorded with CFEs very close to the cell surface (Wightman, Jankowski et al. 1991; Chow, Rüden et al. 1992; Wightman, Schroeder et al. 1995). The amperometric signals for a given exocytotic event measured with an ECD array differ among different electrodes in their time course depending on the fusion pore-electrode distance. However, the largest amperometric signal of a given event is recorded by the closest electrode and thus has a similarly short half-width. As a criterion that all electrodes of an ECD array are equally sensitive we thus require that each electrode gave at least one amperometric spike with a half-width < 20 ms. If one of the electrodes measured no or only small and slow signals during an experiment, the experiment was discarded.

Electrochemical imaging has several advantages over fluorescence imaging. It selectively images exocytotic events at the cell surface. Although this is also possible using total internal reflection fluorescence (TIRF) microscopy (Steyer and Almers 1999), the electrochemical imaging has much higher time resolution. Our recordings filtered at 500 Hz were about 10 times faster than video rate, and at higher bandwidth

sub-millisecond time resolution is possible. The high time resolution and signal-to-noise ratio allows detection of amperometric foot signals (Chow, Rüden et al. 1992), which reflect the opening and expansion of the exocytotic fusion pore (Albillos, Dernick et al. 1997). Thus, using ECD arrays electrochemical imaging of fusion pore opening and expansion can be performed with high temporal and spatial resolution. In contrast, it has yet been impossible to detect the opening of the initial narrow fusion pore by fluorescence techniques.

Exocytosis in neuronal cell types critically depends on so-called SNARE proteins in the vesicle and the plasma membrane (Söllner, Whiteheart et al. 1993).Interactions of these proteins may be directly involved in the fusion event (Chen, Scales et al. 1999; Weber, Parlati et al. 2000), but direct evidence is yet to be obtained and alternative hypotheses have been put forward (Morel 2003). Conformational changes in the SNARE complex can be observed using fluorescence microscopy (An and Almers 2004). It will thus be of great interest to image simultaneously the opening and expansion of individual fusion pores and to correlate the fusion pore dynamics with fluorescence of tagged proteins.

3.5.2. Kinetics of Quantal Release

Quantal release of catecholamines is usually measured using a carbon fiber electrode (CFE) positioned very close to the cell surface (Wightman, Jankowski et al. 1991; Chow, Rüden et al. 1992). It was found that for cell-CFE distances of 5 µm, the individual amperometric spikes were well reproduced by the diffusion kinetics. However, for small distance < 1 µm, spikes were broader than expected for diffusion (Wightman, Schroeder et al. 1995). This was interpreted to reflect release from the vesicle being rate-limiting, reflecting dissociation of catecholamines from the vesicular matrix (Wightman, Schroeder et al. 1995). However, spikes measured very

close to the cell surface were also well reproduced assuming a reduced diffusion coefficient of 3 $x10^{-7}$ cm^2/s near the cell surface (Chow, Rüden et al. 1992).

The experiments with the ECD array described here allow us to distinguish directly between these two possibilities. The diffusion to the electrodes occurs over relatively large distances along the cell surface. If diffusion were normal, as in free solution, then the deconvolution fit of Figure 3.4A would have provided the release function reflecting dissociation of catecholamines form the granular matrix. However, this approach did not provide a satisfactory fit of the measured signals. In contrast, good fits were obtained when a significantly lower diffusion coefficient was used (Figure 3.4B). The half-width of the release function for this event was only 8 ms, which is an overestimate due to the 500 Hz low pass filter. The time course of amperometric spikes measured with a CFE near the cell surface is thus largely determined by a low diffusion coefficient of catecholamines near the cell surface rather than by slow dissociation form the granular matrix.

A low apparent diffusion coefficient is produced if the diffusing molecules bind reversibly to the cell membrane (Hochstrate and Ruppel 1980). The binding mechanisms that reduce the apparent diffusion coefficient near the cell surface are currently unknown. ECD array recordings as described here may be performed on cells pre-treated with proteases to obtain information on the involvement of proteins in catecholamine binding to the cell surface. In addition, reversible binding of catecholamine to the phospholipid bilayer or the glycocalyx that surrounds the cell may be involved. Pre-treatment of the cells with a series of endoglycosidases may thus also provide interesting information.

3.5.3 Future ECD Array Developments and Applications

In the experiments described here cells were placed on the ECD array using a patch pipette. A difficulty with this procedure is that cells must be detached from the surface, a step that often disrupts the cell. To overcome this limitation, cells may be targeted to ECD arrays by other means. Cells may be directed to microelectrode arrays by dielectrophoresis (Gray, Tan et al. 2004) and preliminary experiments in our laboratory indicate that the ECD array itself can be used to trap cells in the ECD center. Using this method we anticipate a significant increase in throughput. Another limitation is that typically only one out of three arrays worked well, i.e. all electrodes were sensitive and exhibited low noise. We recently succeeded in replacing the photoresist insulation by fused silica (SiO_2) insulation creating more robust devices which show low noise more consistently. The fused silica surface also opens the possibility to guiding neuronal and other cell growth on surfaces using surface chemical patterning as previously described for directing growth to electrodes recording electrical activity at multiple sites (James, Spence et al. 2004).

3.6 Acknowledgements

We thank Lori Kwan and Joan Lenz for the cell preparations and excellent technical assistance. This work was supported by the Nanobiotechnology Center (an STC program of the NSF under Agreement No. ECS-9876771) and NIH (RO1 NS38200). It was performed in part at the Cornell Nanofabrication Facility (a member of the National Nanofabrication Users Network) which is supported by NSF under Grant ECS-9731293, its users, Cornell University and Industrial Affiliates.

REFERENCES

Albillos, A., G. Dernick, et al. (1997). "The exocytotic event in chromaffin cells revealed by patch amperometry." Nature **389**(6650): 509-12.

Alés, E., L. Tabares, et al. (1999). "High calcium concentrations shift the mode of exocytosis to the kiss-and-run mechanism." Nature Cell Biology **1**: 40-44.

Almers, W. (1990). "Exocytosis." Annual Reviews of Physiology **52**: 607-624.

An, S. J. and W. Almers (2004). "Tracking SNARE complex formation in live endocrine cells." Science **306**(5698): 1042-6.

Avery, J., D. J. Ellis, et al. (2000). "A cell-free system for regulated exocytosis in PC12 cells." J Cell Biol **148**(2): 317-24.

Chen, Y. A., S. J. Scales, et al. (1999). "SNARE complex formation is triggered by Ca^{2+} and drives membrane fusion." Cell **97**: 165-174.

Chow, R. H., L. v. Rüden, et al. (1992). "Delay in vesicle fusion revealed by electrochemical monitoring of single secretory events in adrenal chromaffin cells." Nature **356**: 60-63.

Dernick, G., G. Alvarez de Toledo, et al. (2003). "Exocytosis of single chromaffin granules in cell-free inside-out membrane patches." Nat Cell Biol **5**(4): 358-62.

Dias, A. F., G. Dernick, et al. (2002). "An electrochemical detector array to study cell biology on the nanoscale." Nanotechnology **13**: 285-289.

Gerhardt, G. A. and R. N. Adams (1982). "Determination of diffusion coefficients by flow injection analysis." Analytical Chemistry **54**: 2618-2620.

Gray, D. S., J. L. Tan, et al. (2004). "Dielectrophoretic registration of living cells to a microelectrode array." Biosens Bioelectron **19**(12): 1765-74.

Hamill, O. P., A. Marty, et al. (1981). "Improved patch-clamp technique for high-resolution current recording from cells and cell-free membrane patches." Pflügers Archiv European Journal of Physiology **391**: 85-100.

Hochstrate, P. and H. Ruppel (1980). "On the evaluation of photoreceptor properties by micro-fluorimetric measurements of fluorochrome diffusion." Biophys Struct Mech **6**(2): 125-38.

James, C. D., A. J. Spence, et al. (2004). "Extracellular recordings from patterned neuronal networks using planar microelectrode arrays." IEEE Trans Biomed Eng **51**(9): 1640-8.

Lindau, M. and G. Alvarez de Toledo (2003). "The fusion pore." Biochim Biophys Acta **1641**(2-3): 167-173.

Morel, N. (2003). "Neurotransmitter release: the dark side of the vacuolar-H(+)ATPase." Biol Cell **95**(7): 453-7.

Parsons, T. D., J. R. Coorssen, et al. (1995). "Docked granules, the exocytic burst, and the need for ATP hydrolysis in endocrine cells." Neuron **15**(5): 1085-96.

Söllner, T., S. Whiteheart, et al. (1993). "SNAP receptors implicated in vesicle targeting and fusion." Nature (London) **362**: 318-323.

Steyer, J. A. and W. Almers (1999). "Tracking single secretory granules in live chromaffin cells by evanescent-field fluorescence microscopy." Biophys J **76**(4): 2262-71.

Tabares, L., E. Ales, et al. (2001). "Exocytosis of catecholamine-containing and catecholamine-free granules in chromaffin cells." J Biol Chem **276**: 39974-39979.

Weber, T., F. Parlati, et al. (2000). "SNAREpins are functionally resistant to disruption by NSF and alphaSNAP." J Cell Biol **149**(5): 1063-72.

Wightman, R. M., J. A. Jankowski, et al. (1991). "Temporally resolved catecholamine spikes correspond to single vesicle release from individual chromaffin cells."

Proceedings of the National Academy of Sciences of the United States of America **88**: 10754-10758.

Wightman, R. M., T. J. Schroeder, et al. (1995). "Time course of release of catecholamines from individual vesicles during exocytosis at adrenal medullary cells." Biophysical Journal **68**: 383-390.

Williams, R. M. and W. W. Webb (2000). "Single granule pH cycling in antigen-induced mast cell secretion." J Cell Sci **113**: 3839-50.

Zhou, Z., S. Misler, et al. (1996). "Rapid fluctuations in transmitter release from single vesicles in bovine adrenal chromaffin cells." Biophysical Journal **70**: 1543-1552.

CHAPTER 4

SIMULTANEOUS OBSERVATION OF EXOCYTOSIS VIA AMPEROMETRIC DETECTION AND FLUORESCENCE RELEASE USING TRANSPARENT MICROELECTRODES AND TIRF MICROSCOPY*

4.1 Abstract

We have developed and tested transparent microelectrode arrays capable of simultaneous amperometric measurement of oxidizable molecules and fluorescence imaging through the electrodes. Electrodes were microfabricated from either indium-tin-oxide (ITO), a transparent conducting material, or very thin (~12-17 nm) gold films on glass substrates. Chromaffin cells loaded with lysotracker green or acridine orange dye (Invitrogen, Carlsbad, CA) were placed atop the electrodes and imaged with total internal reflection fluorescence (TIRF) microscopy while catecholamine from single vesicles was measured concurrently with the electrodes. Both materials were capable of detecting amperometric signals with high resolution. Upon comparing the amperometric signals measured by either ITO or gold electrodes with similar dimensions, we found that on average events recorded with ITO electrodes had about half the amplitude and detected half as much charge as signals detected with gold electrodes, while the amperometric signal half widths were of similar duration. This indicates that the ITO electrodes are not as sensitive as gold electrodes for measurement of quantal catecholamine release. The lower sensitivity is presumably due to reduction of the ITO during catecholamine oxidation (Monk and Man 1999).

* Research presented in this chapter was performed in collaboration with Brian Kim, who assisted in device fabrication and data aquisition, Khajak Berberian who assisted with various computer simulations, and Qinghua Fang who performed the cell culture work. It is my intention to publish this work in a peer reviewed journal.

4.2 Introduction

Neurons release transmitter molecules in a process called exocytosis, wherein membrane bound packets, or vesicles, storing transmitter molecules release their contents into the extracellular space upon stimulation. Many cell types share this release mechanism, including adrenal chromaffin cells, which release the catecholamines adrenaline and nor-adrenaline (Coupland 1965). Chromaffin cells are widely used as a model system to study exocytosis. Release of catecholamine from chromaffin cells can be measured using the electrochemical technique of amperometry, typically using a carbon fiber electrode (Wightman, Jankowski et al. 1991a; Wightman, Jankowski et al. 1991b). Upon oxidization, each catecholamine molecule transfers two electrons to the amperometric electrode. Release from single vesicles is indicated by an amperometric current spike (Wightman, Jankowski et al. 1991b), often preceded by a foot signal (Chow, Rüden et al. 1992) indicating opening and expansion of the fusion pore (Albillos, Dernick et al. 1997).

To gain information about the exocytotic mechanism, it is desirable to perform simultaneous fluorescence imaging and electrochemical detection of individual release events. We previously demonstrated that amperometric signals can be measured using opaque platinum microelectrodes patterned on a glass coverslip while simultaneously viewing the release events from labeled vesicles between the electrodes with fluorescence microscopy on an inverted microscope (Hafez, Kisler et al. 2005). However, to detect the maximum electrochemical signal and minimize diffusional broadening, it is desirable to have the electrode in close contact with the release site on the cell membrane, which prohibits observation of the same membrane area by fluorescence microscopy whether carbon fiber electrodes or opaque surface patterned electrodes are used.

Here, we describe and provide a characterization of transparent planar electrochemical detectors fabricated on glass coverslips using standard photolithography techniques. These electrodes are capable of simultaneous amperometry and fluorescence imaging *through* the electrodes using total internal reflection fluorescence (TIRF) microscopy. Transparent planar microelectrode arrays were fabricated from either indium tin oxide (ITO) (Sun and Gillis 2006), a transparent conductive material commonly used in flat screen displays, or thin gold films. Gold is one of few metals that can be made thin enough to be partially transparent in the visible range while maintaining its conductivity and corrosion resistance.

With both electrode materials, single release events could be detected amperometrically, including foot signals, indicating the opening and expansion of individual fusion pores. Simultaneously, release from dye-loaded vesicles could be imaged through the transparent electrodes using TIRF microscopy. We found that amperometric signals measured with transparent gold electrodes were consistent with those measured by carbon fiber or microfabricated platinum electrodes. In contrast, ITO electrodes detected only about half as much charge as transparent gold electrodes, presumably due to reduction of the ITO by some of the electrons it is meant to detect.

4.3 Materials and Methods

4.3.1 Cell Culture

Cells were prepared as described by Parsons, et al (Parsons, Coorssen et al. 1995), and plated on clean 8 mm coverslips. For experiments, coverslips with bovine adrenal chromaffin cells were rinsed with experimental buffer solution ("buffer") consisting of (in mM): 140 NaCl, 5 KCl, 5 $CaCl_2$, 2 $MgCl_2$, 10 HEPES, 10.36-10.41 D-Glucose (pH = 7.22-7.27, Osm = 297-304 mOsm). Coverslips were then placed on a corner of an

electrode array, and covered, along with the electrodes, with ~150 μL of buffer. Individual healthy looking cells were lifted from the coverslips using a glass micropipette and placed onto electrodes, pressing gently with the pipette tips to stimulate the cells (Hafez, Kisler et al. 2005). For fluorescence experiments, cells were incubated in buffer with 3 μM lysotracker green or acridine orange dye (Invitrogen, Carlsbad, CA) for 10 minutes at room temperature, then rinsed with buffer prior to placing the coverslips on the electrode arrays. Cells were used on days 2-5 in culture for experiments involving fluorescence detection, and days 2-3 for the single-electrode comparison experiments.

4.3.2 ITO Electrode Fabrication

ITO-coated #1.5 glass cover slips (10 ohms per square, approx. 150-200 nm thick ITO, 33.1 mm diameter) were purchased from Bioptechs, Inc. (Butler, PA), and patterned using standard photolithography and wet etch techniques in a clean room environment. Coverslips were cleaned with acetone and isopropanol, spin-coated with Shipley S1813 (Marlborough, MA) photoresist (4000 rpm for 30 sec), then pre-baked on a 115 °C hot plate for 60 sec, resulting in a layer of resist approximately 1 μm thick. Conductor patterns were transferred to the resist from custom made masks via contact photolithography using either an ABM (San Jose, CA) or Karl Suss MA6 (Waterbury Center, VT) contact aligner. After exposure the pattern was developed by immersing the coverslips in MF-322 (Shipley) for 20 seconds. The coverslips were then post-baked on a hot plate for 60 sec at 130-135 °C and descumed in an ozone cleaner (Samco UV-1, Sunnyvale, CA) for one minute to remove any resist residue left behind by the developer in preparation for etching.

The ITO left exposed was then etched away in a solution of 6 M HCl and 0.2 M $FeCl_3$ (Chen, Gao et al. 2007) for 40 minutes. The resist was removed by soaking

the coverslips into Microposit 1165 Photoresist Remover (Shipley) for one minute, exposing the ITO conductor pattern. A second layer of photoresist, spun from S1805 (Shipley) resist to ~0.4 μm thickness was patterned, developed, and descumed as above on top of the ITO conductors to act as an insulation layer, leaving exposed only the conductor tips, which act as the active electrodes. As a side effect, the ozone reportedly enhances the ITO conductivity (Kim, Friend et al. 1999). The resulting electrode arrays were then put through a final post-bake on a 130-135 °C hotplate for 60 sec. Coverslips were cut to 25 mm squares with a wafer saw (K&S 7100, Fort Washington PA) or by hand with a diamond scribe before or after fabrication, respectively. Conductive paint (Silver Print II, GC Electronics, Rockford, IL) was applied to the electrode contact pads to enhance the electrical connection to the amperometric amplifiers.

Electrode arrays were fabricated in two different geometries. One geometry consisted of four ITO electrodes located at the corners of an approximately 12 μm square. Individual electrodes had active areas between ~15 to 48 μm^2. In the other geometry single electrodes were approximately circular with active areas of ~12.5 μm^2 exposed near the tips of 10 μm wide wires. Examples of both electrode geometries are shown schematically in Figure 4.1A and B. Examples of ITO electrodes fabricated in both four- and single-electrode geometries are shown in Figure 4.1C and D, respectively.

4.3.3 Transparent Gold Electrode Fabrication

Transparent gold microelectrodes were fabricated in a cleanroom environment using standard lithography and lift-off techniques on 25 mm square #1.5 thickness glass coverslips (0211 glass, Corning Inc., Corning, NY). Coverslips were cleaned with

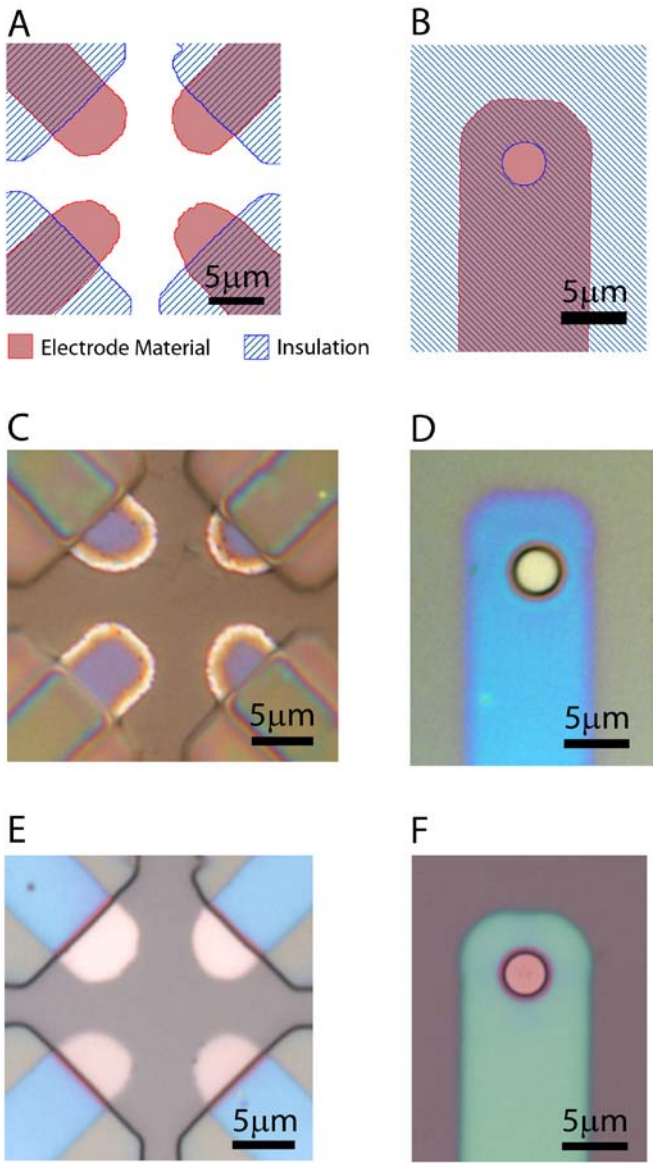

Figure 4.1. Transparent amperometric electrode geometries. A and B: Schematic diagrams of the typical electrode geometries fabricated. ITO and gold electrodes were fabricated in both four-electrode (A) and single-electrode (B) geometries. Electrodes are indicated in red and the insulation (photoresist) in a blue pattern. C and D: Color differential interference contrast (DIC) images of ITO four- and single-electrode devices fabricated on glass coverslips. The bright fringes around the edges of the ITO electrodes in (C) are caused by a change in thickness near the edges of the electrodes due to the fabrication process. ITO is ~90% transparent. E and F: Color DIC images of ultrathin gold electrodes fabricated in both geometries on glass coverslips. The gold layer was ~12-17 nm thick and ~70% transparent.

acetone and isopropanol. P-20 photoresist primer (Microsi, Inc, Phoenix, AZ) and S1813 resist were spun onto the coverslip, then pre-baked and patterned as for ITO. The "tone" of the exposed pattern was reversed using an NH_3 image reversal oven (YES 58SM, Livermore, CA), and subsequent exposure of the coverslip to 405nm light for 60 seconds. The pattern was developed in MF-321 (Shipley) for one minute, post-baked as for the ITO arrays, and then descumed in an ozone cleaner for 60 seconds. Metals were evaporated onto the coverslips using E-beam evaporation (CVC 4500, Veeco, Plainview, NY), or sputtering (Bal-Tec SCD050, Brookline, NH). A ~2 nm thick adhesion layer of Cr, Ti, or Cu was deposited onto the coverslip, followed by a layer of gold.

Excess metal was lifted off the coverslip with the photoresist by immersing the patterned coverslip in Microposit-1165 remover for 2 hours or more, leaving only the metal electrode array pattern on the coverslips. Occasionally after lift off, some of the excess metal had to be removed by wiping gently with a cleanroom wipe soaked in acetone. Coverslips were again cleaned with acetone and isopropanol, coated with P-20 primer and S1805 photoresist, pre-baked, patterned, and developed as for the ITO arrays above to create an insulation layer. The resulting electrodes had similar geometries and dimensions as the ITO devices (Figure 4.1A and B). Examples of four- and single-electrode transparent gold devices are shown in Figure 4.1E and F, respectively. The final thickness of the metal films were between 12-17nm, determined by AFM (Veeco Dimension 3100, Woodbury, NY). Transparency of the gold films was determined using a UV/Vis/Near-IR spectrophotometer (Shimadzu UV-3101PC, Columbia, MD).

4.3.4 Electrochemical Recording and Analysis

Electrochemical measurements were made as described previously for Platinum ECD arrays (Hafez, Kisler et al. 2005) using a four-channel amperometric amplifier (VA-10M, NPI, Tamm, Germany). Unless otherwise indicated, electrodes were held at 700 mV vs. Ag|AgCl reference electrode, and data was low pass filtered at 500 Hz and acquired at a 5 kHz sampling frequency. If needed, amperometric recordings were digitally filtered with a 60 Hz notch filter to remove line frequency noise using Igor Filter Design Lab 4 for Igor Pro (WaveMetrics, Lake Oswego, OR). Peak height, halfwidth, and quantal size data was determined for all non-overlapping amperometric spikes with amplitude > 2 pA using Mosharov's Amperometric Peak Analysis software (Mosharov and Sulzer 2005) written for Igor Pro, version 7.7. Each cell analyzed had a minimum of four analyzable events. Student's T-tests were used to determine significance between spike parameters for ITO and gold. For characterization of amperometric spikes recorded by ITO and Gold electrodes only unlabeled cells were used (see *Results* and *Discussion* sections).

4.3.5 TIRF Imaging

A modified inverted Zeiss Axiovert 135 TV microscope capable of objective-based TIRF, epi-fluorescence, and bright field imaging was used for these experiments (see Chapter 2). It employs a mercury arc lamp, and annular blocker placed at a plane conjugate to the back focal plane (BFP) of the objective such that it blocks out all "non-critical" light for TIRF mode (Axelrod 2001). A Zeiss plan-fluar 1.45 NA 100x oil emersion objective was used to observe the bottom of the cells in TIRF illumination. 20x and 40x Zeiss air objectives, with or without optivar, were used to observe cells in brightfield and for positioning purposes. For TIRF experiments, illumination was provided by a 100 W Hg arc lamp (HBO 100W/3, Osram, Danvers,

MA), with 480/40 nm excitation, 505 nm dichroic, and 535/30 nm emission filters (Chroma Technology, Rockingham, VT). Images were recorded using an Andor iXon EMCCD camera (South Windsor, CT) and accompanying iXon software. The camera output signal was also recorded in order to sync image sequences with the amperometric data. One to three sequences of 2000 frames were taken during each fluorescence experiment. Frame acquisition times were 49.76-50.78 ms, with a 1.8 ms interframe time. With the 100x objective, image pixels scaled to 165 nm per pixel.

4.3.6 Image Analysis

With lysotracker green, which accumulates in acidic compartments such as chromaffin granules, a release event was indicated by a sudden decrease in the fluorescence of the vesicle. Acridine orange also accumulates in acidic compartments, but at concentrations such that the fluorescence is partially quenched (Williams and Webb 2000). A release event from an acridine orange labeled vesicle is indicated by a brief bright flash as the fluorescent dye dequenches upon leaving the vesicle (Steyer, Horstmann et al. 1997; Avery, Ellis et al. 2000).

Difference images were used to determine the location and timing of release events in the fluorescence images, using custom written programs in V++ as described (Hafez, Kisler et al. 2005). Briefly, the average of ten images immediately prior to a sequence of six images of interest was subtracted from those six images. With lysotracker green, a release event was indicated in the difference images by a sudden localized intensity decrease that persisted over at least three frames. With Acridine Orange, a release event was indicated by a transient fluorescence increase (flash) due to the dye dequenching as it was released from the vesicle.

The precise contours of four-electrode ITO arrays used in fluorescence experiments were determined by AFM and then matched to fluorescence images to

properly locate the fluorescently labeled vesicles relative to the electrodes: A 2000 frame average image of a fluorescence sequence was obtained using V++ (Digital Optics, Auckland, New Zealand). Both the AFM image and the average fluorescence image were scaled to the same pixel size in Photoshop 6.0 (Adobe, San Jose, CA) and then aligned to each other. The edges of the electrodes were defined by the AFM image, which had higher resolution. The contours of four-electrode gold arrays could be determined from a 2000 frame average image from a fluorescence image sequence. For display purposes, images were contrast adjusted and either median filtered or gaussian filtered (r = 0.5 pixels) in Photoshop.

4.4 Results

Examples of amperometric events detected with ITO and transparent gold four-electrode arrays are shown in Figure 4.2. These recordings were made with the cells placed in the center of the arrays, sitting atop sets of four electrodes (Figure 4.1A), such that amperometric events that occurred between the electrodes were detected in more than one electrode. Each electrode is represented by a different color, and the amplitude of the event recorded by each electrode depends upon the proximity of the electrode to the vesicle release site (Dias, Dernick et al. 2002; Hafez, Kisler et al. 2005). The larger current responses clearly reveal a pre-spike feature, also called a foot signal. The onset of the foot signal indicates the opening of a narrow fusion pore (arrowhead O in Figure 4.2). The onset of the amperometric spike corresponds to the rapid expansion of the fusion pore (Albillos, Dernick et al. 1997).

Exocytotic release events detected amperometrically by ITO or transparent gold were in several cases associated with a fluorescence change observed simultaneously by TIRF microscopy (Figure 4.3, Figure 4.4). Figure 4.3, Top, shows an amperometric event recorded with an ITO electrode array from a lysotracker green

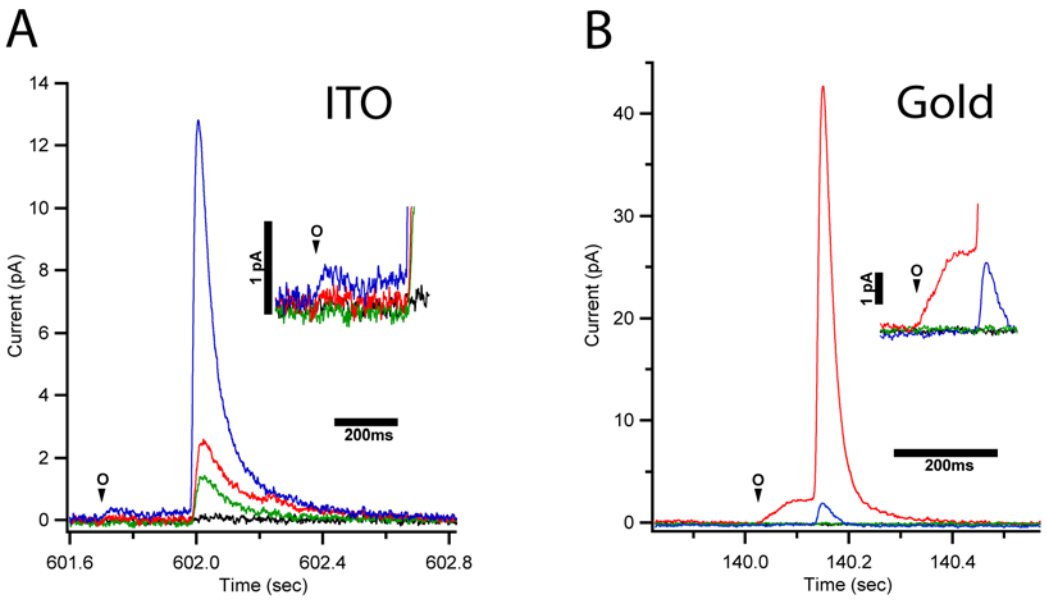

Figure 4.2. Amperometric events recorded with ITO and transparent gold four-electrode arrays. Each color represents one of the four electrodes in the array, detecting the event simultaneously. The size of the event detected by a given electrode depends upon its proximity to the release location on the cell surface. Note the foot signals indicating the initial onset of exocytosis were detected in one or more of the electrodes. Insets: Foot signals shown on expanded vertical scales. Traces were smoothed for display purposes.

labeled cell together with a sequence of the corresponding TIRF images of the cell surface (Figure 4.3, Middle). The difference images, which reveal the changes in fluorescence more clearly (Figure 4.3, Bottom), show a sudden localized loss of fluorescence as the appearance of a dark spot. This loss of fluorescence reflects release of the fluorescent dye from the vesicle together with the catecholamine that was detected amperometrically.

Figure 4.4, Top, shows an amperometric event recorded by a single transparent gold electrode from a cell loaded with acridine orange. In the corresponding TIRF image sequence (Figure 4.4, Middle) and more clearly in the difference image

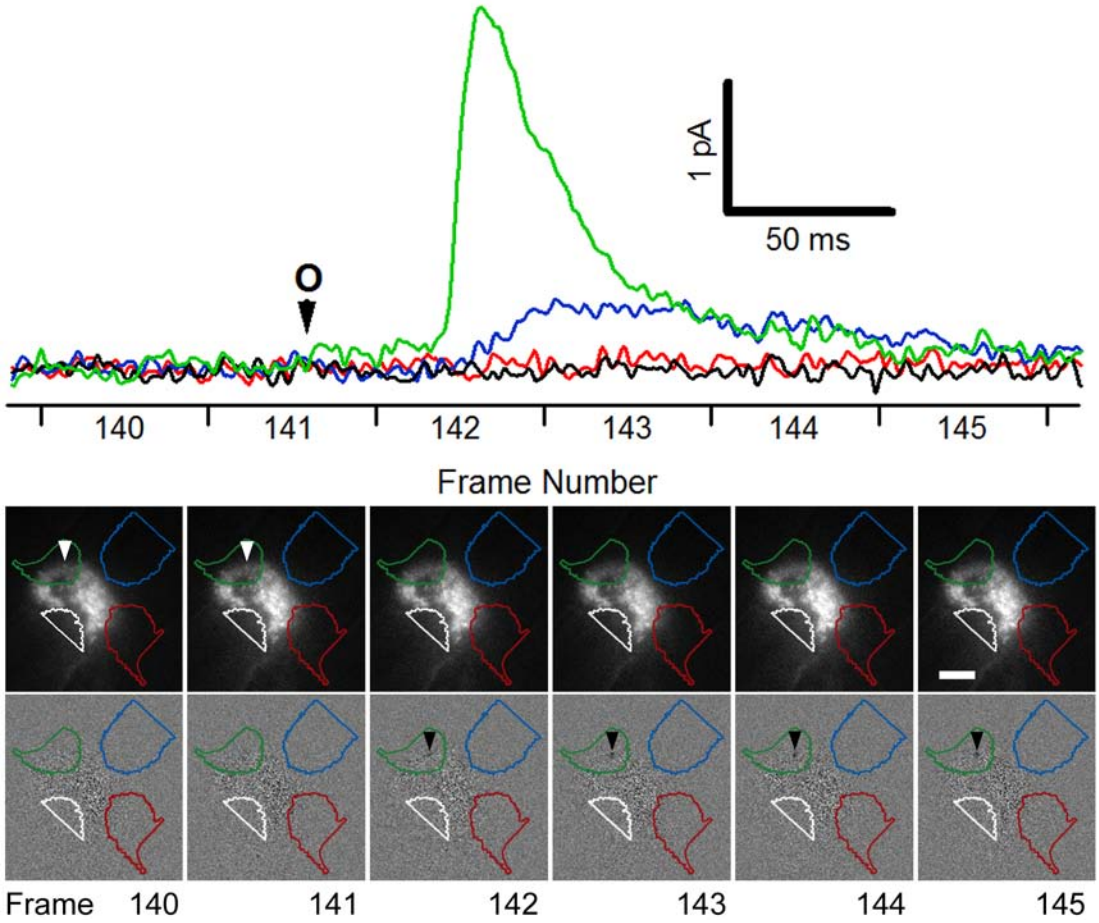

Figure 4.3. Correlation of amperometric and fluorescence information for a single release event over ITO electrodes. Top: An exocytotic event from a chromaffin cell recorded with four-electrode ITO array. The event was detected primarily by the electrode represented in green. The initial opening of the fusion pore foot signal is visible in the green trace and indicated by the "O" and arrow. The timing of the image sequence is indicated below the current trace. Middle: TIRF images and their corresponding difference images (Bottom) of the cell loaded with lysotracker green dye atop the electrode array. Each electrode is outlined in the color corresponding to its current trace. The arrows in the TIRF and difference images indicate the presence of a vesicle in frames 140-141, followed by a dark spot appearing over the "green" electrode in the difference images starting in frame 142, indicating loss of fluorescence from a vesicle, which in turn indicates exocytosis. The spot appears at the same time that the current rapidly increases in the amperometric recording (frame 142). Exposure times were 50 ms; scale bar is 5 μm. Amperometric traces were smoothed for display.

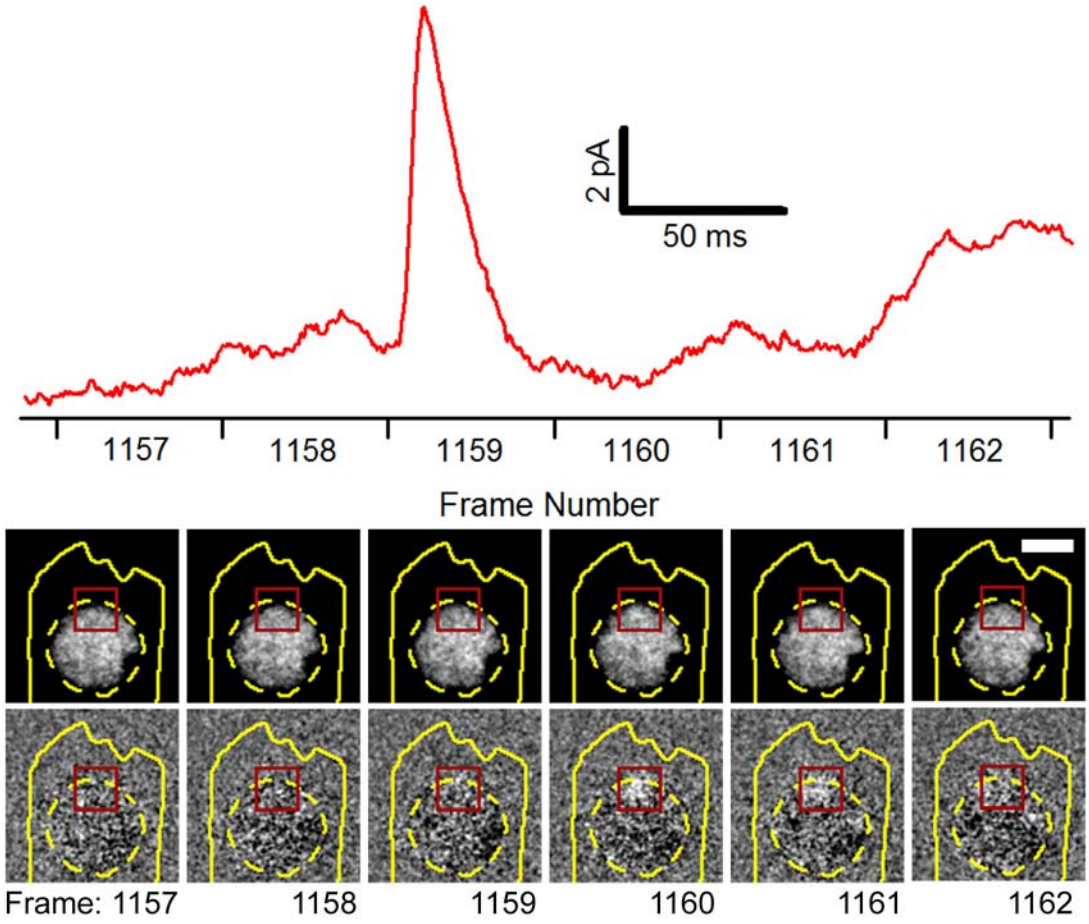

Figure 4.4. Correlation of amperometric and fluorescence information for a single release event over a transparent gold electrode. Top: An exocytotic release event from a chromaffin cell recorded with a single transparent gold electrode. The timing of the image sequence is indicated below the current trace. TIRF (Middle) and difference (Bottom) images of the cell atop the electrode showing a bright flash inside the red square, appearing in the frame immediately after the rapid increase in current (frame 1160), indicating release. The electrode wire was outlined in yellow, with the active electrode area outlined by the dashed yellow line. The cell was stained with Acridine Orange dye, which generates a bright dequenching flash upon release from vesicles. Exposure times were 50 ms; scale bar is 5 μm. Amperometric trace was smoothed for display.

sequence (Figure 4.4, Bottom), exocytosis of the fluorescent dye is indicated by a bright flash due to the dye dequenching as it was released.

When analyzing lysotracker green fluorescence sequences, there was often also some fluorescent brightening of the vesicle in the frame immediately prior to the frame in which the release event occurred (data not shown). The frame in which the main intensity decrease was observed in the difference images was usually the frame during which the steep rising phase of the amperometric spike occurred, with few exceptions. In contrast, when acridine orange was used, the initial fluorescence flash typically occurred in the frame immediately following the frame during which the rising phase of the amperometric spike occurred. This delay is presumably due to the extra time needed for acridine orange to de-aggregate (Clerc and Barenholz 1998) and dequench. In the difference images the frames in which the release event occurred are all compared to the same ten frames preceding the sequence. Therefore the vesicles labeled with lysotracker green must have been present at the membrane for most or all of these preceding ten frames. Thus, for these cells only exocytosis of vesicles that have been tethered at the membrane for at least 0.5 sec could be reliably detected in the fluorescence images.

Single ~12.5 μm^2 electrodes (Figure 4.1B) were used to evaluate the detection efficiency of ITO compared to transparent gold. Events detected by ITO and gold electrodes yielded average quantal charges of 0.48±0.10 pC and 1.11±0.24 pC, average amperometric spike amplitudes of 14.4±2.7 pA and 6.7±1.2 pA, and average amperometric spike half-widths of 69.2±14.7 ms and 52.4±5.5 ms, respectively (Figure 4.5A-C). The differences in charge and amplitude of the amperometric spikes between ITO and gold electrodes indicate that ITO is less efficient for catecholamine

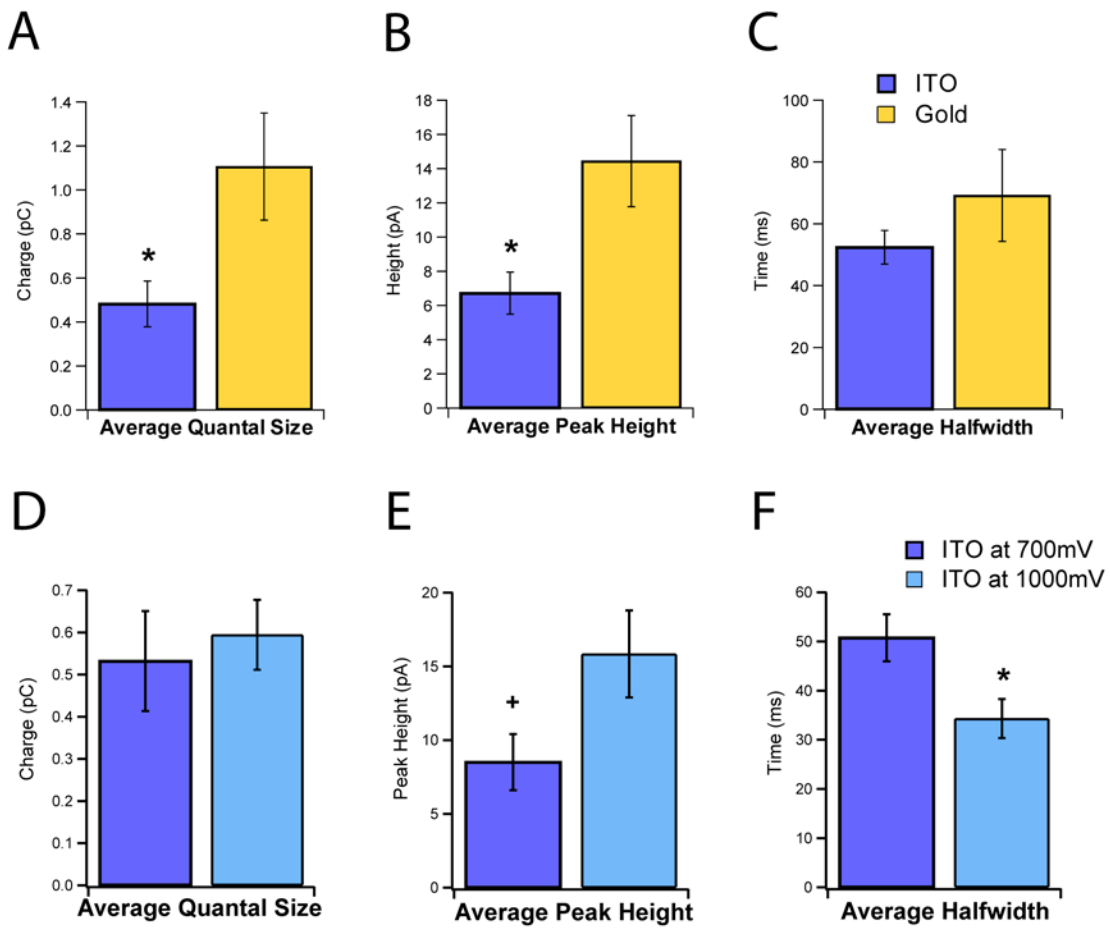

Figure 4.5. Comparison of amperometric events recorded with ITO and gold single-electrodes of similar geometry. (A-C) ITO vs. transparent gold electrodes: ITO electrodes seem to detect only about half as much charge, on average, with peaks roughly half the height (B) as those detected with ultrathin gold electrodes with similar geometry. This indicates that ITO is less efficient at oxidizing catecholamine molecules then gold. However, the average spike width is not significantly different for ITO and Gold (C). This implies that some of the electrons generated during oxidation at ITO electrodes may be lost somewhere between oxidation and the recording apparatus. N = 13 cells for ITO and 9 for gold. (D-F) Comparison of amperometric events recorded with ITO single electrodes at 700 mV and 1000 mV (N = 7 and 8 cells, respectively). The charge measured by the ITO electrodes at the two potentials are very similar (D), even though the events recorded at 1000 mV tended to be taller (E) and faster (F) then those recorded at 700 mV on average. This suggests that 700 mV is sufficient for ITO to oxidize catecholamine effectively. * indicates $p < 0.02$, + indicates $p < 0.07$. Error is ±SEM.

detection than transparent gold. However, the average halfwidths for the two materials are very similar. This suggests that some of the electrons generated during catecholamine oxidation are lost before they can be detected by the recording apparatus.

Because ITO is a doped semiconductor, it can be susceptible to voltage drops across the contacts used to supply voltage to the ITO electrodes due to the difference in work functions of the ITO and metal contacts, sometimes called “non-ohmic” connections. This would cause the potential at the ITO electrode to be lower than the normally applied potential. If the potential drop were large enough, it could result in incomplete oxidation of catecholamines. We thus compared the amperometric signals detected by ITO electrodes at our standard potential of 700 mV to those detected with ITO electrodes held at 1000 mV. Data from single ITO electrodes held at 700 and 1000 mV yielded average amperometric spike charges of 0.53±0.12 pC and 0.59±0.08 pC, average amplitudes of 8.5±1.9 pA and 15.8±2.9 pA, and amperometric spike half widths of 50.8±4.8 ms and 34.3±4.0 ms, respectively, (Figure 4.5D-F). While the kinetics of the oxidation reaction were apparently accelerated at 1000 mV, there was no significant difference in the quantity of catecholamines (amperometric spike charge) detected. This indicates that applying a potential of 700 mV to the ITO was sufficient to oxidize the catecholamines.

4.5 Discussion

We demonstrated the ability to detect amperometric events using low noise transparent ITO and ultrathin gold microelectrodes. Foot signals (Figure 4.2 insets) were also detected with both ITO and gold electrodes, indicating that these materials are capable of detecting narrow fusion pores, the initial stages of exocytosis. Furthermore, we can see the release of fluorescent dye from vesicles undergoing exocytosis under TIRF

illumination *through* the electrodes as the amperometric data is collected simultaneously. Figure 4.3 and Figure 4.4 illustrate simultaneous fluorescence and amperometric detection of exocytosis using ITO and gold electrodes, respectively.

While it has been reported that ITO and noble metals such as gold and platinum (Dias, Dernick et al. 2002; Hafez, Kisler et al. 2005; Sun and Gillis 2006) have detected amperometric signals consistent with those detected by carbon fibers, there are significant differences between the behaviors of these materials. Qualitatively ITO and gold electrodes generate similar information about the exocytotic events detected. Quantitatively, as shown in Figure 4.5A, ITO electrodes detect on average only about half as much charge as gold electrodes ($p = 0.016$). Further, amperometric spikes recorded with ITO electrodes had on average about half the amplitude as those detected with gold electrodes ($p = 0.008$). However, the half widths are not significantly different for the two materials (Figure 4.5C), implying that the charge may be lost somewhere between catecholamine oxidation and the recording apparatus, while the kinetics of detection are unchanged.

One possibility is that there is a voltage drop at the connection to the ITO electrode, due to a difference in the work functions of the ITO and metal (gold in our case) connector. If the voltage drop were large enough, the potential at the electrode may not be adequate to efficiently oxidize the catecholamine. If that were the case, increasing the potential applied to the electrode would increase the efficiency of the electrode, resulting in larger measured quantal size. When we compared events recorded at 700 mV to those at 1000 mV, we did observe a change in the shape of the current spikes. The amperometric spikes recorded at a potential of 1000 mV had a larger amplitude ($p = 0.064$, Figure 4.5E) and shorter half width ($p = 0.019$, Figure 4.5F) on average than those recorded at 700 mV. However, there was no significant change in the average quantal size ($p = 0.667$, Figure 4.5D). Although the difference

in average amplitude between events recorded at 700 and 1000 mV fell short statistical significance, the results clearly indicate that holding the ITO electrode at a higher potential increased the speed at which oxidation occurs, but not the sensitivity. Therefore ITO's lower efficiency is due to some other inherent material property, not a drop in voltage at the connection point.

It is possible that the catecholamines are oxidized at the ITO surface as with gold or other noble metals, but some of the electrons and H^+ generated in the reaction in turn react with the ITO surface, reducing the ITO itself (Monk and Man 1999). As a doped semiconductor, ITO's conductivity depends on the amount of tin in the In_2O_3 and defects in the oxide lattice (Monk and Man 1999). Thus, changes to the oxide composition can have significant effects. Some of the electrons and H^+ released during catecholamine oxidation may react with the ITO surface, absorbing the electrons and possibly reducing the ITO to a less conductive state. These reactions may depend on many subtle factors, including pH (Folcher, Cachet et al. 1997; Monk and Man 1999), Cl^- concentration (Folcher, Cachet et al. 1997), and electrode potential. Gold, being a pure metal, tends not to suffer from these effects as profoundly as ITO.

With the gold electrodes, one can take advantage of surface plasmon resonance (SPR), and/or metal-enhanced fluorescence (MEF) (Lakowicz 2005). SPR enhances the excitation illumination in the vicinity of the metal surface, but quenches fluorescence very close (within the 2-8 nm) to the gold surface. MEF enhances the fluorescence signal from fluorophores near the metal surface. These effects are compatible with TIRF illumination, and helps compensate for gold's lower transparency compared to ITO. Yet, transparent gold has its own drawbacks. Because of the small thickness necessary for light transmission, the gold films are not as mechanically robust as the thicker films of ITO. For example, voltage spikes on the order of 1V unintentionally applied to the gold electrodes can cause the metal to peel

off the coverslip surface. Careful device design and choice of adhesion layer has helped offset this shortcoming.

For applications requiring a high degree of transparency or mechanical robustness, and that can tolerate reduced catecholamine detection efficiency, ITO may be a good choice of material. If one requires high amperometric sensitivity, and ~70% transparency (possibly augmented with SPR) is acceptable, ultrathin gold is a better choice of electrode material.

4.6 Acknowledgements

I thank Joan Lenz for her excellent technical support and assistance, and to Jonathan Shu of the Cornell Center for Nanoscale Systems and the Cornell Center for Materials Research for assistance with the AFM and spectrophotometer. This material is based upon work supported in part by the Nanobiotechnology Center, an STC Program of the National Science Foundation under Agreement No. ECS-9876771, and NIH grants RO1 NS38200, T32GM007469. This work was performed in part at the Cornell NanoScale Facility, a member of the National Nanotechnology Infrastructure Network, which is supported by the National Science Foundation (Grant ECS-0335765).

REFERENCES

Albillos, A., G. Dernick, et al. (1997). "The exocytotic event in chromaffin cells revealed by patch amperometry." Nature **389**: 509-512.

Avery, J., D. J. Ellis, et al. (2000). "A cell-free system for regulated exocytosis in PC12 cells." J Cell Biol **148**(2): 317-24.

Axelrod, D. (2001). "Selective imaging of surface fluorescence with very high aperture microscope objectives." J Biomed Opt **6**(1): 6-13.

Chen, X. H., Y. F. Gao, et al. (2007). "Controlled stimulation of quantal catecholarnine release from chromaffln cells using photolysis of caged Ca2+ on transparent ludium-tin-oxide microchip electrodes." Biophysical Journal: 86a-86a.

Chow, R. H., L. v. Rüden, et al. (1992). "Delay in vesicle fusion revealed by electrochemical monitoring of single secretory events in adrenal chromaffin cells." Nature **356**: 60-63.

Clerc, S. and Y. Barenholz (1998). "A quantitative model for using acridine orange as a transmembrane pH gradient probe." Anal Biochem **259**(1): 104-11.

Coupland, R. E. (1965). The Natural History of the Chromaffin Cell. London, Longmans, Green and Co.

Dias, A. F., G. Dernick, et al. (2002). "An electrochemical detector array to study cell biology on the nanoscale." Nanotechnology **13**: 285-289.

Folcher, G., H. Cachet, et al. (1997). "Anodic corrosion of indium tin oxide films induced by the electrochemical oxidation of chlorides." Thin Solid Films **301**(1-2): 242-248.

Hafez, I., K. Kisler, et al. (2005). "Electrochemical imaging of fusion pore openings by electrochemical detector arrays." Proceedings of the National Academy of Sciences of the United States of America **102**: 13879-13884.

Kim, J. S., R. H. Friend, et al. (1999). "Surface energy and polarity of treated indium-tin-oxide anodes for polymer light-emitting diodes studied by contact-angle measurements." Journal of Applied Physics **86**(5): 2774-2778.

Lakowicz, J. R. (2005). "Radiative decay engineering 5: metal-enhanced fluorescence and plasmon emission." Anal Biochem **337**(2): 171-94.

Monk, P. M. S. and C. M. Man (1999). "Reductive ion insertion into thin-film indium tin oxide (ITO) in aqueous acidic solutions: the effect of leaching of indium from the ITO." Journal of Materials Science-Materials in Electronics **10**(2): 101-107.

Mosharov, E. V. and D. Sulzer (2005). "Analysis of exocytotic events recorded by amperometry." Nat Methods **2**(9): 651-8.

Parsons, T. D., J. R. Coorssen, et al. (1995). "Docked granules, the exocytic burst, and the need for ATP hydrolysis in endocrine cells." Neuron **15**(5): 1085-96.

Steyer, J. A., H. Horstmann, et al. (1997). "Transport, docking and exocytosis of single secretory granules in live chromaffin cells." Nature **388**(6641): 474-8.

Sun, X. and K. D. Gillis (2006). "On-chip amperometric measurement of quantal catecholamine release using transparent indium tin oxide electrodes." Anal Chem **78**(8): 2521-5.

Wightman, R. M., J. A. Jankowski, et al. (1991a). "Temporally resolved catecholamine spikes correspond to single vesicle release from individual chromaffin cells." Proceedings of the National Academy of Sciences of the United States of America **88**: 10754-10758.

Wightman, R. M., J. A. Jankowski, et al. (1991b). "Temporally resolved catecholamine spikes correspond to single vesicle release from individual chromaffin cells." Proc. Natl. Acad. Sci. USA **88**: 10754-10758.

Williams, R. M. and W. W. Webb (2000). "Single granule pH cycling in antigen-induced mast cell secretion." J Cell Sci **113 Pt 21**: 3839-50.

CHAPTER 5

CHARGED C-TERMINAL SYNAPTOBREVIN MUTATIONS NEGATIVELY AFFECT EXOCYTOSIS[*]

5.1 Abstract

To study the specific function of the C-terminal end of synaptobrevin II (SybII), a SNARE protein located in the vesicle membrane, we added charged peptides to the C-terminus of SybII, and a green fluorescent protein (GFP) to the opposite end to track the protein. Either two positively charged lysine (K) peptides were added (GFP-SybII-KK) or two negatively charged glutamic acid (E) peptides (GFP-SybII-EE). A GFP was also added to a wild-type SybII to act as a control. Cells containing these proteins exhibited punctate fluorescence, indicating that the proteins were correctly localized to the vesicles. In cells expressing the wild-type GFP-SybII, disappearance of brightly labeled vesicles could be correlated to amperometric current spikes. For GFP-SybII-KK and GFP-SybII-EE events however, loss of punctate fluorescence could not be correlated to current spikes from the electrochemical detectors. This indicates that vesicles carrying the SybII mutant with added charged residues at the C-terminus are incapable of exocytosis.

5.2 Introduction

Over the past few years there has been much debate and study focused on a set of three proteins: SNAP-25 and syntaxin, both in the plasma membrane of the cell, and synaptobrevin II (SybII), which typically resides in vesicle membranes (Söllner,

[*] This work was performed in collaboration with Annita Ngatchou, who did the cell culture and transfection work, and some of the protein engineering, and Qinghua Fang who did much of the protein engineering and viral vector manipulations. Portions of this chapter have been submitted to a journal for publication.

Whiteheart et al. 1993). These three proteins are selectively cleaved by Tetanus Toxin and Botulinum Neurotoxins (reviewed in (Schiavo, Matteoli et al. 2000)), which revealed their key role in exocytosis. Together, these three proteins are known to form a four-helix coiled-coil motif called the SNARE complex (Sutton, Fasshauer et al. 1998). Evidence suggests that this complex forms starting at the N-termini of the proteins, progressing towards the C-termini in what is termed a "zippering" fashion to bring the vesicle and plasma membranes together and somehow initiate fusion (Sorensen, Wiederhold et al. 2006). However, it still remains unclear how the SNARE proteins could disrupt the membranes to generate a fusion pore between the vesicle and plasma membranes. While much work has been done investigating the cytoplamic SNARE domains and their formation of the coiled-coil motif, there has been little focus on whether the C-terminal and transmembrane regions of SybII and syntaxin play an active role in fusion pore formation.

Many models of SNARE protein zippering have been proposed to explain how forces applied by the SNARE proteins fuse the vesicle and plasma membranes together. Few place much focus on the C-terminal of SybII. Capacitance experiments performed by Ngatchou, et al (Ngatchou, Kisler et al. 2009) using SybII deficient chromaffin cells expressing SybII modified to include one or two additional residues at the C-terminus of the protein revealed that the more polar the residue added to the end of SybII, the less exocytosis occurred. This implies that the SybII C-terminus plays a significant role in force transfer to the vesicle membrane and onset of vesicle fusion.

To determine if the modified proteins were correctly targeted to the vesicle membrane combined Total Internal Reflection Fluorescence (TIRF) microscopy imaging and electrochemical measurements using microfabricated electrochemical

detector (ECD) arrays were performed on wild-type (WT) cells expressing SybII with charged amino acids added to the C-terminus and a GFP label to the N-terminus.

5.3 Methods

5.3.1 Cell Culture and Transfection

Chromaffin cells from young adult WT mice were prepared as described (Sorensen, Matti et al. 2002) and used on days two and three in culture. The SybII protein was modified by the addition of either two lysine (-KK) or two glutamic acid (-EE) peptides to the C-terminus end of SybII, and attachment of a green fluorescent protein (GFP) to the N-terminal of the proteins. A GFP label was also attached to the N-terminus of the unmodified version of SybII to act as control. A schematic of the mutated protein is shown in Figure 5.1. These constructs were inserted into the pSFV (Semliki Forest virus) (Ashery, Betz et al. 1999) vector to enable viral expression of the GFP-SybII, GFP-SybII-KK, or GFP-SybII-EE constructs in the chromaffin cells. Experiments were performed approximately 6 hours after infection (Kesavan, Borisovska et al. 2007).

5.3.2 Total Internal Reflection Fluorescence (TIRF) Microscopy Measurements

An inverted microscope (Axiovert 135 TV, Zeiss, Thornwood, NY) modified for TIRF microscopy as described (Axelrod 2001) and fitted with a Zeiss plan-fluar 1.45

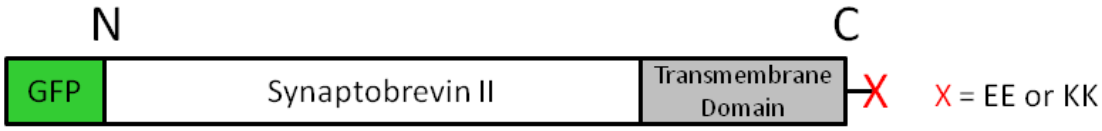

Figure 5.1. Schematic diagram of the Synaptobrevin II protein, indicating where a green fluorescent protein (GFP) and additional charged peptides were added. Not to scale.

NA 100x oil emersion objective was used to observe the cells during experiments. Illumination was provided by a 100W mercury arc lamp (HBO 103W/2, Osram, Danvers, MA), with 480/40 nm excitation filter, 515 nm dichroic, and 520 nm long pass emission filter (Chroma Technology, Rockingham, VT). Images were collected using an EMCCD camera (Andor iXon, South Windsor, CT) and its accompanying software. For each cell, a 2000 frame image sequence was collected. The exposure time for each frame was 100-150 ms, with an interframe time of 1.8 ms.

Prior to each experiment, transfected cells were located using a 20x Zeiss air objective (with or without optivar) under epifluorescence illumination. Transfected cells chosen for study had a characteristic green color due to the GFP labeling, and exhibited a concentration of the label in the ER. The cells of interest were also inspected under bright field illumination to insure healthy cells were chosen.

5.3.3 Electrochemical Detection

Microfabricated platinum electrode (ECD) arrays were used to amperometrically detect the release of catecholamines from the transfected chromaffin cells. Each ECD array consists of a set of four planar Pt electrodes fabricated on a glass coverslip, as described previously (Dias, Dernick et al. 2002; Hafez, Kisler et al. 2005). Briefly, the four electrodes of an ECD reside at the corners of a square sized such that a cell can be placed atop the array and viewed through the glass coverslip while amperometric information is recorded from all four electrodes simultaneously. The ECD arrays were fabricated as described (Dias, Dernick et al. 2002; Hafez, Kisler et al. 2005) except for an improved insulation layer, which was created by chemical vapor deposition of approx. 300 nm of SiO_2 onto the electrodes (IPE 1000 PECVD), and subsequent etching of the SiO_2 layer via reactive ion etching (PlasmaLab 80Plus, Oxford

Instruments, Concord, MA) to expose the active areas of the electrodes and contact pads.

Cells were located to and positioned on the ECD arrays using a micropipette as described (Hafez, Kisler et al. 2005). Amperometric currents due to spontaneous exocytotic events were low pass filtered at 500 Hz, and acquired with 5 kHz sampling rate and analyzed as described (Hafez, Kisler et al. 2005). For analysis, a 5 pA minimum current peak height was used as threshold, with a minimum of four events ≥ 5 pA in height per cell. The camera output signal was recorded in order to synchronize the timing of the fluorescence image frames with electrochemical signals.

5.3.4 Image Analysis

Amperometric events with signals detectable for at least two electrodes were correlated to frames in the corresponding image sequences in order to determine which amperometric events were associated with detectable fluorescence changes. Likely exocytotic events were determined by visual inspection of original TIRF images and difference images using V++ (Digital Optics, Auckland, New Zealand) as described (Hafez, Kisler et al. 2005). Briefly, difference images were created by averaging the ten images immediately prior to a sequence of six images of interest and subtracting that average from those six images. An exocytotic event was defined as a localized loss of intensity that persisted for at least three frames.

For each set of six TIRF images which exhibited a likely exocytotic event in an area consistent with the amperometric signals, the images were further processed in Photoshop (Adobe, San Jose, CA) by applying a Gaussian smoothing filter (r = 0.8). Subsequently all images from all events were adjusted using the same values for gray levels, brightness, and contrast. This made it possible to confirm or reject the disappearance of punctate fluorescence (vesicles) from the image sequences in

conjunction with the amperometric events, and compare exocytotic events from the WT and mutant cells.

5.4 Results

For simultaneous TIRF imaging and electrochemical detection of individual exocytotic events, cells expressing a GFP-SybII construct were manipulated to the center of a four-electrode ECD array. While there was significant diffuse fluorescence across the cell, presumably due to the presence of the fluorescent constructs in the plasma membrane (Wienisch and Klingauf 2006), bright, punctuate fluorescence spots indicating vesicular localization of the protein constructs could also be seen in the infected cells (Figure 5.2). Vesicular movement, indicated by movement of the punctuate spots (Figure 5.3), was frequently observed in many of the infected cells as well.

Exocytotic events at the bottom cell surface manifested themselves as amperometric current spikes recorded by the ECD electrodes (Hafez, Kisler et al. 2005). Eight of nine GFP-SybII expressing cells showed four or more events with amplitude ≥ 5 pA. Figure 5.4A shows amperometric currents that appear in all four

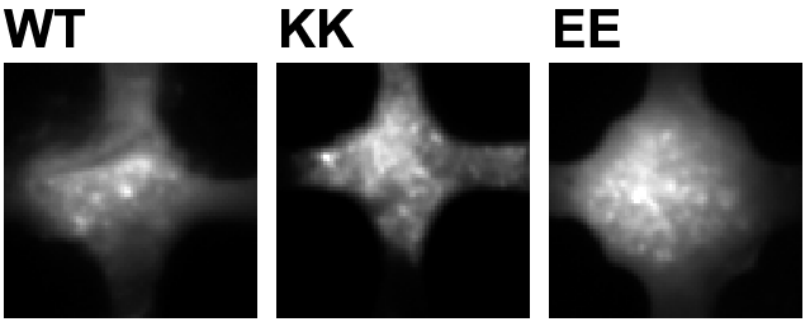

Figure 5.2. Punctate fluorescence of the SybII constructs indicate localization to the vesicles. The diffuse fluorescence is due to the SybII constructs in the plasma membrane and ER or Golgi apparatus from overexpression of the proteins.

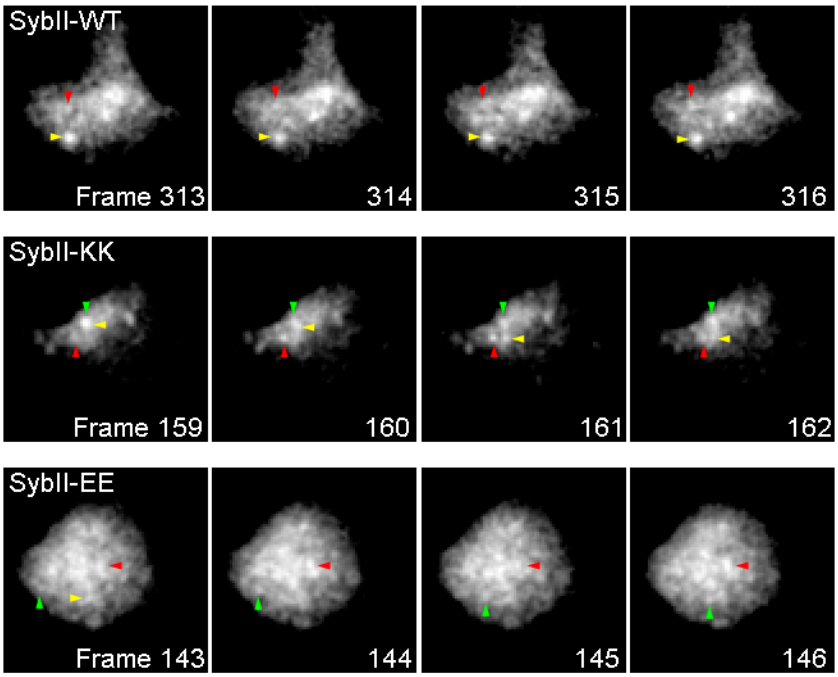

Figure 5.3. Selections from SybII construct TIRF image sequences. Arrows point out a few vesicles. Top: A WT GFP-SybII cell. There is some movement of the vesicle with the red arrow. Middle: A GFP-SybII-KK cell. The vesicle with the yellow arrow moves downwards. Bottom: A GFP-SybII-EE cell. The vesicle indicated by the green arrow moves across the cell.

electrodes of the ECD array but with different amplitudes. The colors of the individual traces refer to the individual electrodes as indicated by the colored dots in the images below. The amperometric current spikes recorded by the electrode with the red dot are largest, indicating that these events occurred near this electrode. Accordingly, the amperometrically detected events were accompanied by the disappearance of fluorescent spots between frames 539-540 (red arrow) and 541-542 (blue arrow). The disappearance of these spots at these locations is consistent with fusion of these vesicles with the plasma membrane and diffusion of the GFP-SybII away from the vesicle membrane into the plasma membrane. With GPF-SybII expressing cells 18 events showed a measureable amperometric current in multiple electrodes, which allows localization of the event (Hafez, Kisler et al. 2005), associated with apparent

Figure 5.4. Vesicular localization of SybII-KK and SybII-EE. (A-C) Simultaneous ECD array amperometry and TIRF microscopy imaging of wild type cells expressing GFP-SybII (A), GFP-SybII-EE (B) and GFP-SybII-KK (C). Scale bars are 2 µm. Colors of amperometric traces (top panels) correspond to the respective electrodes as indicated by colored dots in images below. Frame acquisition timing for image sequences are indicated below the amperometric traces. In a GFP-SybII cell (A), two amperometric events detected by multiple electrodes of the ECD array are associated with loss of fluorescence puncta between frames 539-540 (red arrow) and 541-542 (blue arrow). The area in the yellow rectangle is enlarged in the bottom panel. In a GFP-SybII-EE cell (B) and a GFP-SybII-KK cell (C) amperometric events (top) are not associated with loss of fluorescence puncta in TIRF images (bottom). The lower images are enlargements of the area enclosed by the yellow rectangles indicating the general area where fluorescence release should have been observed.

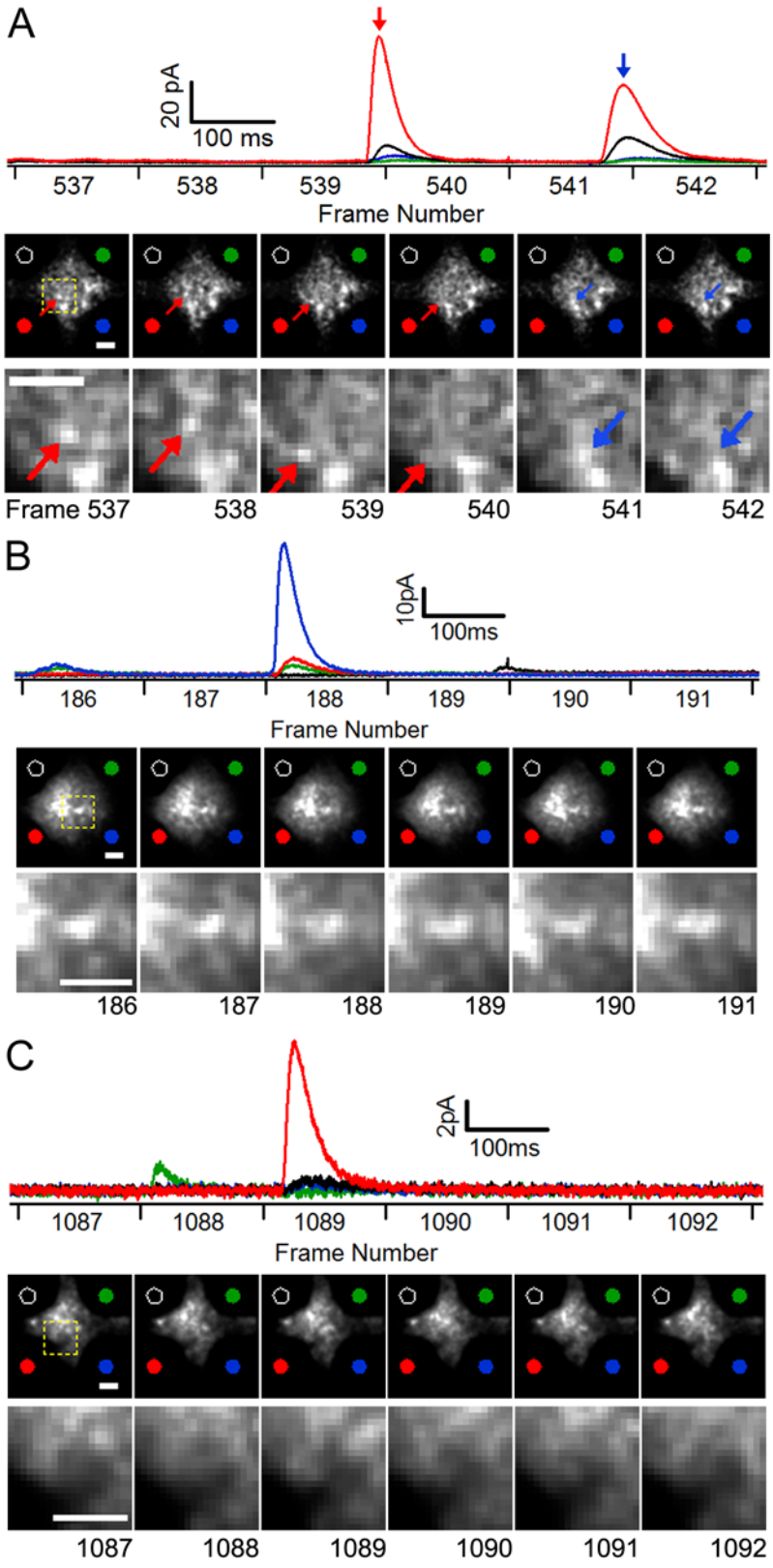
A
20 pA
100 ms
537
538
539
540
541
542
Frame Number
Frame 537
538
539
540
541
542
B
10pA
100ms
186
187
188
189
190
191
Frame Number
186
187
188
189
190
191
C
2pA
100ms
1087
1088
1089
1090
1091
1092
Frame Number
1087
1088
1089
1090
1091
1092

loss of fluorescence. Five of these events (28%) had an associated disappearing fluorescent vesicle in the expected region.

When cells expressing GFP-SybII-EE were used (Figure 5.4B), only three out of eight cells showed four or more amperometric spikes with amplitude ≥ 5 pA. None of the events that could be localized from the electrochemical data (10) could be correlated to the disappearance of a fluorescent vesicle. Six of eight GFP-SybII-KK expressing cells (Figure 5.4C) showed four or more events ≥ 5 pA. Out of seven events that could be localized from the amperometric data only one showed a disappearing vesicle in the expected region.

SybII-KK amperometric events were significantly smaller then WT events. Average charge, peak-height, and half width for the WT and mutant SybII cells are compared in Table 5.1. Averages were calculated as means of the medians per cell, in order to reduce cell to cell variability and the influence of outlier data points.

5.5 Discussion

The punctuate fluorescence observed in the infected cells indicates that GFP-SybII, GFP-SybII-KK, and GFP-SybII-EE protein constructs each localize to vesicles. Further evidence of vesicular localization comes from the size of these punctate spots (~300-450 nm across) and their movement near the bottom of the cells (Figure 5.3).

Table 5.1. Average amperometric spike parameters. Error is ± SEM. Charge, half width, and peak height were calculated as means of the medians. *p < 0.02, **p<0.007 vs. WT using Student's T test.

Construct	Charge (pC)	Half Width (ms)	Peak Height (pA)	No. Events
SybII WT (n=8)	0.6529 ± 0.0623	29.22 ± 3.31	12.55 ± 0.55	63 ± 17
SybII-KK (n=6)	0.4042 ± 0.0254 **	24.22 ± 1.70	9.983 ± 0.747 *	33 ± 16
SybII-EE (n=3)	0.5829 ± 0.0711	25.49 ± 1.65	12.04 ± 1.00	85 ± 30

While the GFP-SybII-KK and GFP-SybII-EE mutants do localize to vesicles, the lack of disappearance of bright, punctate fluorescent vesicles that correspond to amperometric signals, compared to GFP-SybII-WT (Figure 5.4), indicates that GFP-SybII-KK and GFP-SybII-EE are unlikely to support exocytotic events. The addition of the charged residues to the SybII C-terminus thus inhibits exocytosis.

However, the amperometric data indicates that when these proteins are expressed in WT chromaffin cells, that exocytosis still occurs. On average, the number of events per cell in cells with four or more analyzable events was similar for both the WT and mutant SybII constructs. The endogenous WT proteins in the cells are most likely responsible for fusion pore formation in cells expressing GFP-SybII-KK or GFP-SybII-EE. This interpretation is strongly supported by the observation that the amperometric events in these cells did not reflect exocytosis of fluorescent vesicles, in contrast to GFP-SybII expressing cells.

It is interesting to note that the average quantal size, amperometric peak height, and half-width for cells overexpressing GFP-SybII-EE were very similar to those expressing GFP-SybII-WT, while the GFP-SybII-KK events had significantly smaller quantal size and peak height then WT, as shown in Table 5.1. Because an ECD array was used to detect the molecules, it is highly likely that the ECD detected most of the molecules released in each exocytotic event. Therefore, a difference in quantal size (and corresponding peak height) indicates that the GFP-SybII-KK cells released fewer molecules per vesicle then WT, on average.

This reduction in quantal size could be due to incomplete release of the catecholamines contained within the vesicles, a change in catecholamine concentration within the vesicles, or a change in vesicle size. Let us first consider incomplete release of catecholamine. It is fairly well established that there are two basic modes of exocytosis: the ‘full fusion’ mode, where the complete contents of the vesicle are

released and the vesicle membrane is incorporated into the plasma membrane. And the transient fusion mode, sometimes referred to as ‘cavicapture’ or ‘kiss-and-run,’ where a fusion pore opens only briefly between the vesicle and plasma membrane, resulting in partial release of the vesicle contents (Taraska and Almers 2004). Furthermore, it has been shown recently that under low stimulation conditions, the mode of exocytosis could shift to the more transitory form (Fulop, Radabaugh et al. 2005). However, because cells containing the three different SybII protein constructs were stimulated under the same conditions, a shift towards transient fusion would have to be related to expression of the specific SybII constructs

Exocytosis in GFP-SybII-KK expressing cells occurred primarily from vesicles that did not contain the fluorescent GFP-SybII-KK construct. Given that there is a large amount of the SybII protein overexpressed in the plasma membrane with these constructs, it is likely that even vesicles that are not discernibly labeled with the fluorescent SybII construct may still contain some GFP-SybII-KK. Because multiple SNAREs are required for fusion (the current estimate lies between 3-15 according to a review by Montecucco, et al (Montecucco, Schiavo et al. 2005)) the SybII-KK protein present in the vesicle could become involved in a SNARE complex and fusion event in concert with the endogenous SybII. In this case, the positive charges at the C-terminal of GFP-SybII-KK may act to impair the ability of the other (endogenous) proteins to open a sufficiently stable fusion pore to proceed to full vesicle fusion. Or, the positive charges on GFP-SybII-KK may electrostatically constrict the opening through which the positively-charged catecholamines would flow. These two effects are not mutually exclusive, and some combination of these effects could create a more severe impact on fusion pore opening and expansion then either would alone. I would expect a similar effect if the GFP-SybII-KK in the plasma membrane took the place of syntaxin in some SNARE complexes. Support for this comes from a report of

recombinant SybII and SNAP-25 complex formation (Fasshauer, Eliason et al. 1998). Electrostatic hindrance and destabilization of the fusion pore may not occur with the SybII-EE mutant because the C-terminal charges are negative, and the glutamic acid could possibly be protonated due to the acidity inside the vesicle or the charge shielded by some of the catecholamine molecules.

Alternatively, the SybII-KK mutant may have some effect on the contents of the vesicle. Chromogranin proteins found in chromaffin vesicles are thought to be responsible for binding large quantities of catecholamines to themselves, creating a highly concentrated matrix of protein-bound catecholamines. Further, it has been shown recently that the absence of chromogranin A reduces the quantity of catecholamine exocytosed per vesicle (Montesinos, Machado et al. 2008). In the SybII-KK protein, the lysine (K) side chain terminates in the same way as norepinepherine, with a chain of carbon atoms terminating in a positively-charged amino group. While little is known about how catecholamines bind to chromogranins, the similarities between lysine and norepinephrine suggest that the lysines at the end of SybII-KK may interact with chromogranin to disrupt or inhibit catecholamine binding and/or matrix formation. However, this effect would be limited since the lysines would protrude into the vesicle no more then 1 nm.

Because the lysines are basic, SybII-KK could also raise the pH locally inside the vesicle, where the pH is typically around 5.5. This is supported by data indicating that alkali molecules displace catecholamines inside vesicles (Machado, Gomez et al. 2002; Camacho, Machado et al. 2006). Again, this effect would be limited because of the reach of the lysine peptides into the vesicle. Their reach could be great enough to affect the VMAT (vesicular monoamine transporter) protein, responsible for pumping catecholamines into vesicles, though. The VMAT transporter is pH dependant and anchored in the vesicle membrane (Colliver, Pyott et al. 2000; Eiden, Schafer et al.

2004), making it more likely to encounter the lysines of a SybII-KK molecule. Because the VMAT protein pumps H^+ out of the vesicle in exchange for catecholamine, a locally higher pH would result in less efficient transport of catecholamine into the vesicle.

In conclusion, C-terminal addition of the charged residues EE or KK to SybII strongly inhibits exocytosis. Vesicles carrying these constructs very rarely fuse with the plasma membrane, in contrast to WT GFP-SybII. In far less concentrated quantities, GFP-SybII-KK and GFP-SybII-EE may participate in exocytosis with endogenous SybII, but in a nonproductive or inhibitory manner. The expression of GFP-SybII-KK protein construct also decreases quantal size, possibly causing instabilities in the fusion pore or changes to the interior of the vesicle that reduce the average number of molecules released per vesicle. It remains to be established if the reduction in quantal size is linked to a change in vesicle size form this data. Experiments using patch amperometry or electron microscopy could provide the information needed to answer that question.

5.6 Acknowledgements

I thank Joan Lenz for excellent technical assistance. I am also grateful to Manfred Lindau and Annita Ngatchou for many helpful discussions and critical reading of this chapter. This work was supported by the Nanobiotechnology Center (an STC program of NSF Agreement No. ECS-9876771) and NIH (RO1 NS38200, R01GM085808, T32GM007469). It was performed in part at the Cornell Nanofabrication Facility (a member of the National Nanofabrication Users Network) which is supported by NSF under Grant ECS-9731293, its users, Cornell University and Industrial Affiliates.

REFERENCES

Ashery, U., A. Betz, et al. (1999). "An efficient method for infection of adrenal chromaffin cells using the Semliki Forest virus gene expression system." Eur J Cell Biol **78**(8): 525-32.

Axelrod, D. (2001). "Total internal reflection fluorescence microscopy in cell biology." Traffic **2**(11): 764-74.

Camacho, M., J. D. Machado, et al. (2006). "Intragranular pH rapidly modulates exocytosis in adrenal chromaffin cells." J Neurochem **96**(2): 324-34.

Colliver, T. L., S. J. Pyott, et al. (2000). "VMAT-Mediated changes in quantal size and vesicular volume." J Neurosci **20**(14): 5276-82.

Dias, A. F., G. Dernick, et al. (2002). "An electrochemical detector array to study cell biology on the nanoscale." Nanotechnology **13**: 285-289.

Eiden, L. E., M. K. Schafer, et al. (2004). "The vesicular amine transporter family (SLC18): amine/proton antiporters required for vesicular accumulation and regulated exocytotic secretion of monoamines and acetylcholine." Pflugers Arch **447**(5): 636-40.

Fasshauer, D., W. K. Eliason, et al. (1998). "Identification of a minimal core of the synaptic SNARE complex sufficient for reversible assembly and disassembly." Biochemistry **37**(29): 10354-62.

Fulop, T., S. Radabaugh, et al. (2005). "Activity-dependent differential transmitter release in mouse adrenal chromaffin cells." J Neurosci **25**(32): 7324-32.

Hafez, I., K. Kisler, et al. (2005). "Electrochemical imaging of fusion pore openings by electrochemical detector arrays." Proc Natl Acad Sci U S A **102**(39): 13879-84.

Kesavan, J., M. Borisovska, et al. (2007). "v-SNARE actions during Ca(2+)-triggered exocytosis." Cell **131**(2): 351-63.

Machado, J. D., J. F. Gomez, et al. (2002). "Hydralazine reduces the quantal size of secretory events by displacement of catecholamines from adrenomedullary chromaffin secretory vesicles." Circ Res **91**(9): 830-6.

Montecucco, C., G. Schiavo, et al. (2005). "SNARE complexes and neuroexocytosis: how many, how close?" Trends Biochem Sci **30**(7): 367-72.

Montesinos, M. S., J. D. Machado, et al. (2008). "The crucial role of chromogranins in storage and exocytosis revealed using chromaffin cells from chromogranin A null mouse." J Neurosci **28**(13): 3350-8.

Ngatchou, A., K. Kisler, et al. (2009). "Movement of Synaptobrevin C-terminus Induces Fusion Pore Formation." Submitted.

Schiavo, G., M. Matteoli, et al. (2000). "Neurotoxins affecting neuroexocytosis." Physiol Rev **80**(2): 717-66.

Söllner, T., S. Whiteheart, et al. (1993). "SNAP receptors implicated in vesicle targeting and fusion." Nature (London) **362**: 318-323.

Sorensen, J. B., U. Matti, et al. (2002). "The SNARE protein SNAP-25 is linked to fast calcium triggering of exocytosis." Proc Natl Acad Sci U S A **99**(3): 1627-32.

Sorensen, J. B., K. Wiederhold, et al. (2006). "Sequential N- to C-terminal SNARE complex assembly drives priming and fusion of secretory vesicles." Embo J **25**(5): 955-66.

Sutton, R. B., D. Fasshauer, et al. (1998). "Crystal structure of a SNARE complex involved in synaptic exocytosis at 2.4 Å resolution." Nature **395**: 347-353.

Taraska, J. W. and W. Almers (2004). "Bilayers merge even when exocytosis is transient." Proc Natl Acad Sci U S A **101**(23): 8780-5.

Wienisch, M. and J. Klingauf (2006). "Vesicular proteins exocytosed and subsequently retrieved by compensatory endocytosis are nonidentical." Nat Neurosci **9**(8): 1019-27.

CHAPTER 6

A NOVEL CELL DETECTION TECHNIQUE USING SINGLE WALLED CARBON NANOTUBES*

6.1 Abstract

Single walled carbon nanotubes (CNTs) were utilized as electrolyte-gated field effect transistors to study interactions between living cells and unmodified CNTs. Devices employing CNTs lying directly on the substrate did not respond to cells placed atop the devices. However, when cells were placed on nanotubes suspended over a trench, significant shifts in nanotube conductance and gate voltage dependence were observed in response to cell placement. The results suggest that suspended CNTs may insert into the hydrophobic core of the cell membrane where they are stabilized by hydrophobic interactions.

6.2 Introduction

Carbon nanotubes (CNTs) have received considerable attention since their discovery in 1991 (Iijima 1991), with their potential for applications in many scientific fields. They are small yet strong, can be semiconducting or metallic, and are made from one of the most common substances on the surface of the earth: carbon. A single walled CNT can be thought of as a sheet of graphene rolled up and joined into a cylinder approximately 1-2 nm in diameter. All CNTs are hydrophobic. CNT devices have been used to detect small molecules and DNA in solution (Gruner 2006; Larrimore, Nad et al. 2006; Trojanowicz 2006). Recently, the interaction of lipids with CNTs has been investigated using lipid membranes in cell-free systems (Bradley, Davis et al.

* The research in this section was performed in collaboration with Lisa Larrimore and Samantha Roberts, both of whom created nanotube devices and assisted in data acquisition. Lisa Larrimore performed the photocurrent measurements as well.

2005; Zhou, Moran-Mirabal et al. 2007), or using the lipids as surfactants to render the CNTs soluble in water (Richard, Balavoine et al. 2003). However, no studies have been reported that investigate the interaction of pristine CNTs with living cells.

In detection devices utilizing CNTs to create field effect transistors (Bachtold, Hadley et al. 2001), the ends of the CNT are connected to source and drain electrodes, and a gate voltage can be applied via a back gate or water gate (Rosenblatt, Yaish et al. 2002) to control whether the transistor is "on" or "off" (conducting or nonconducting, respectively). Molecules of interest are detected as conductance and threshold voltage changes in the transistor. In the experiments presented here, p-type single walled CNTs were utilized to form transistors that could be gated by an electrode placed in a salt buffer covering the devices. We observed changes in the conductance and gate dependence of these transistors in the presence of chromaffin cells from the adrenal gland or mast cells (responsible for histamine release and found throughout the body) under specific conditions.

6.3 Materials and Methods

6.3.1 Cell Culture

Chromaffin cells were obtained as described (Parsons, Coorssen et al. 1995) and plated on 8 mm coverslips. For experiments, coverslips with adhering cells were rinsed with an external buffer solution consisting of (in mM): 150 NaCl, 5 KCl, 5 $CaCl_2$, 2 $MgCl_2$, and 10 HEPES with a pH of 7.25 and osmolarity of 313 mOsm. The cell-dotted coverslip was then placed near the CNT device. Cells and the active area of the CNT device were covered with a 50-100 μL droplet of buffer. Cells were used on days 2-5 in culture.

For fluorescence measurements, cells were incubated in buffer containing 3 μm FM1-43 (Molecular Probes/Invitrogen, Carlsbad, CA) for 10 minutes at room

temperature prior to the experiment. FM1-43 is a lipophilic probe that accumulates and becomes fluorescent in cell membranes. An equilibrium exists between the probes in solution and those in the cell membrane, so to maintain plasma membrane staining, the dye must be continuously present in the buffer.

Rat mast cells were a kind gift from Jose Moran-Mirabal of the Craighead group. These cells were obtained suspended in media, and were pelleted via centrifugation (500G for 5min) and resuspended in the external buffer solution. For some experiments, the cells were provided pre-labeled with DiI-C_{18}-3, another lipophilic dye. For experiments, 50-100 μL of the suspension was placed on a device coverslip, and the cells were allowed to settle to the bottom. Cells were used on day one in culture.

6.3.2 Device Fabrication

CNT transistor devices were fabricated on thin (~170 μm thick) fused silica coverslips as described (Larrimore 2008), based on the method of (Larrimore, Nad et al. 2006). Briefly, single-walled semiconducting carbon nanotubes were grown on the fused silica from photolithographically defined catalyst sites. Source and drain electrodes were patterned from Pt, Au, or Pd using standard photolithography techniques. The source and drain electrodes were spaced 10 μm apart. Because of the difference in Fermi level between the metal contacts and CNTs, the CNTs behave as p-type semiconductors in these devices. In some devices 1-4 μm wide trenches were etched into the fused silica midway between the source and drain electrodes to create suspended CNT devices (Figure 6.1). An active device, signifying the presence of one or more CNTs connected between the source and drain electrodes, was indicated by a constant nonzero current (I_{SD}) upon application of a voltage across the source and drain electrodes, and a gate voltage (V_g) dependent I_{SD}.

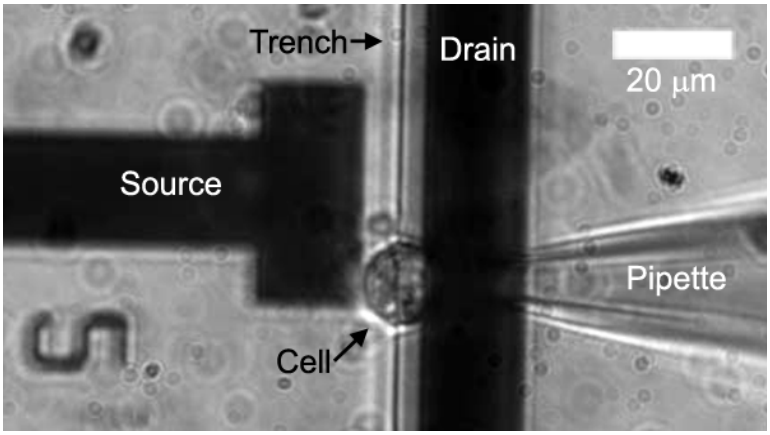

Figure 6.1. Photograph of the experimental configuration using a suspended CNT transistor device. A chromaffin cell was placed onto a CNT (not visible) spanning the distance between the source and drain electrodes using a glass micropipette. Distance between source and drain electrodes is 10 μm. The data presented in Figure 6.4A and B was obtained from the device and cell shown here.

6.3.3 CNT Device Localization

CNTs are not visible with optical microscopy, so their exact locations relative to the source and drain electrodes after device fabrication were unknown. In some devices the position of the CNTs between source and drain electrodes were determined with atomic force microscopy (AFM) or photocurrent measurements (Balasubramanian, Burghard et al. 2005; Ahn, Tsen et al. 2007). In photocurrent microscopy, a focused laser spot is scanned across the area of interest containing one or more CNTs connected to the source and drain electrodes. When the laser moves across a CNT, the CNT behaves as a photovoltaic device. An incoming photon interacts with an electron in the CNT, exciting it from the valence to conduction band, where the excited electrons and holes generated are detected as electrical currents. Because the position of the laser is known at any given time, an image can be formed by plotting current detected vs. laser position (Figure 6.2). Photocurrent measurements are a preferred method because there is less risk of damaging suspended devices compared to AFM,

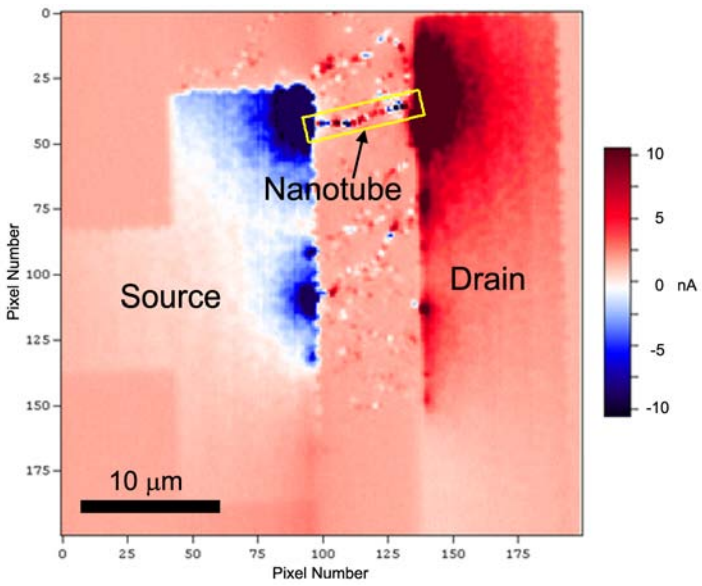

Figure 6.2. An example of photocurrent dec-tection of a CNT in a transistor device. The CNT appears as a distinct line of dots indicating the sign and magnitude of the photocurrent detected along the CNT (due to its band structure) bridging the gap between the source and drain electrodes. Colors indicate the amount of current arising from each pixel in the image. Original image courtesy Samantha Roberts.

and the photocurrent measurements selectively indicate those CNTs that are electrically connected to the source and drain electrodes.

6.3.4 Data Acquisition and Analysis

CNT devices were mounted on an inverted microscope (Zeiss Axiovert 135TV), equipped for annular total internal reflection fluorescence (TIRF) microscopy (see Chapter 2), and viewed in brightfield with a 20x or 40x objective. TIRF measurements were performed with a 100x 1.45 NA objective.

For current (I_{SD}) vs. time measurements, a constant voltage between 2.5 mV and 11 mV, depending upon device, was applied between the source and drain electrodes (V_{SD}). A constant V_g between 0 mV and -300 mV was applied to the devices via a gold or Ag/AgCl wire in contact with the bath solution. The current (I_{SD})

was amplified (Ithaco, Ithaca, NY), sampled by an A-to-D converter at 100 Hz, and stored in a computer. I_{SD} was monitored over time during the course of the experiment and controlled by custom written "measureit" software (Sazonova 2006) in LabView (National Instruments, Austin, TX).

Before and after placement of a cell on a CNT device, which occurred during the I_{SD} vs. time measurement, a "gate voltage sweep" was applied, sweeping V_g between -0.5 V to 0.5 V and measuring the I_{SD} response. This established the gate dependence of the device in the absence and presence of a cell.

In each experiment, a cell was picked up from the coverslip using a glass micropipette, lowered and gently pressed onto the CNT device of interest. In most experiments, the cells were placed randomly between the source and drain electrodes, as the exact location of the CNT spanning the device was unknown. In a few later experiments, AFM imaging or photocurrent measurements were acquired prior to the experiments in order to determine the position of the CNTs of interest.

Subsequently, current measurements (I_{SD}) were converted to conductance (G) to remove variances due to different V_{SD} voltages using the relation:

$$G = {I_{SD}}/{V_{SD}}. \quad (6.1)$$

6.4 Results

In the first experiments cells were placed on non-suspended CNTs laid directly on the substrate between the source and drain electrodes. However, non-suspended CNTs did not react to the presence of a cell. No changes were observed in the conductance or its dependence on V_g when a cell was placed on the device (n = 4). An example is shown in Figure 6.3.

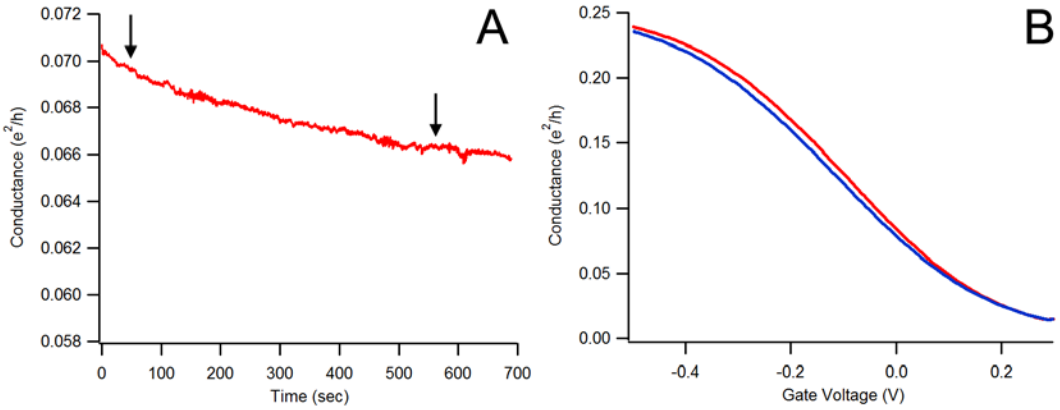

Figure 6.3. Cell interaction with a non-suspended carbon nanotube. (A) Conductance vs. time recorded for a non-suspended CNT transistor. The arrows indicate the approximate times a cell touched down on the CNT transistor. There are no sharp drops in conductance indicating interaction with a CNT, just a slow decay over time due to the evaporation of the buffer solution. (B) V_g dependence of the device used in (A) before (red) and after (blue) cell placement, indicating no change in V_{th}.

In contrast, CNTs suspended over trenches in the substrate respond strongly to cell placement. Changes in conductance vs. time and vs. V_g dependence were observed after placement of a cell atop a CNT in 7 out of 14 successful experiments (50%). Considering that most of these experiments were performed on devices where the precise locations of the CNTs had not been determined by AFM or photocurrent measurements, this is an impressive success rate. In six of the seven successful experiments, the conductance decreased with time upon cell placement, and the dependence on V_g shifted to more negative voltages. The seventh experiment, an anomaly, showed the opposite reaction to the cell. Examples of these changes are given in Figure 6.4. The interaction of the cell with the CNT was not an instantaneous process. Conductance drops took approximately 5 to 95 seconds to reach their final value after the cell was placed on the device. The anomalous device required ~250 seconds to reach its final, higher, conductivity value.

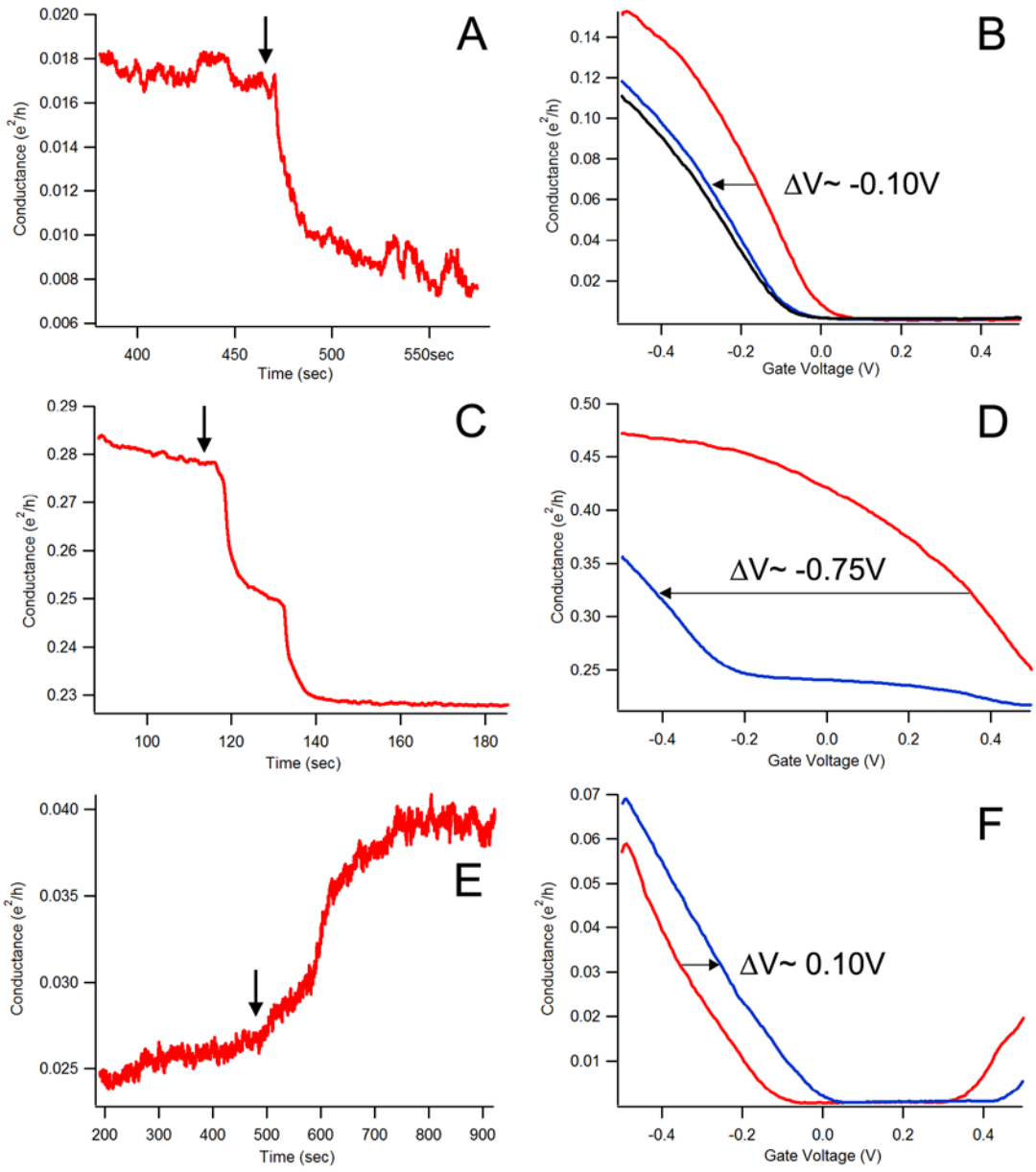

Figure 6.4. Interactions of suspended CNTs with cells. (A) Conductance vs. time recorded for a suspended CNT transistor. The arrow indicates the approximate time a cell was placed on the CNT transistor. A large drop in conductance is observed over ~30 second period shortly after cell placement. (B) V_g dependence of conductance for the device used in (A) before (red) and after (blue) cell placement and conductance drop. The black trace indicates the gate dependence after cell removal. (C) and (D) Similar to (A) and (B), but with a an unusually large, two step conductance drop and ΔV. (E) and (F) Simiar to (A) and (B), but with a positive ΔV. Conductance change occurs over ~ 250 seconds. This is the only event where positive conductance and ΔV shifts were observed.

Shifts in conductance vs. V_g dependence, indicative of a shift in threshold voltage (V_{th}), were observed in the gate voltage sweep measurements for these seven experiments as well, compared to the sweeps taken before cell placement. V_{th} shifts (ΔV) were determined graphically by shifting the gate sweep trace in the presence of a cell along the V_g axis until it was superimposed upon the gate sweep trace in the presence of buffer only on graphs of conductance vs. V_g. ΔV was then the voltage added or subtracted to generate the overlap. Typical V_{th} shifts were between -0.04 and -0.10 V, although there was one exceptional event with a -0.75 V shift (Figure 6.4D). The anomalous experiment displayed a ΔV of +0.10 V (Figure 6.4F). The average magnitude of ΔV was 0.18 ± 0.09 V and the corresponding magnitude of the conductance change was 0.017 ± 0.005 e^2/h on average (error is ± SEM, n = 7). These effects were irreversible upon removal of the cell, as demonstrated by the black trace in Figure 6.4B, compared to the blue trace in the presence of a cell.

TIRF measurements were made with suspended CNT devices. TIRF images were of poor quality because of the discontinuities and scattering induced by the trenches in the devices. No changes in conductance or V_g dependence was detected in the experiments with FM1-43 labeled cells. These experiments were not included in the 14 successful experiments mentioned above, as it appeared highly likely that the FM1-43 had some effect on the CNTs. One of the DiI-C_{18}-3 labeled mast cells did evoke a response from a CNT, however.

6.5 Discussion

Cells were not found to interact with non-suspended CNT devices, as shown in Figure 6.3 for example. This result is consistent with the observation by Larrimore who reported that amoebae crawling across CNT transistors do not affect the CNT conductance (Larrimore 2008). According to Larrimore (Larrimore 2008), the Debye

screening length for a CNT in a salt buffer at the concentrations used in these experiments is on the order of 1 nm. Anything further away from the CNT would be masked by the ions screening the nanotube. Given that a single walled CNT is typically about 1-2 nm in diameter, it would be reasonable that a cell, with the proteins, receptors, etc. that typically protrude from the plasma membrane, as well as extracellular matrix components, would not get close enough to a CNT lying on the substrate to "see" it at all.

To test this hypothesis, CNT devices were fabricated with trenches underneath portions of the CNTs, creating regions where the CNTs were suspended ~ 1 μm above the substrate. The intention was to create a configuration where, as the cell was pressed down onto the CNT, cell-surface components would be able to protrude into the trench, allowing the membrane to get much closer to and possibly contact the CNT. The results with suspended CNT devices indicate that this was indeed the case. Changes in conductance and V_{th} were often observed in the presence of a cell. Figure 6.4A and B illustrate the typical response to a cell interacting with a CNT. In Figure 6.4A, there was a distinct drop in conductance after a cell was placed atop the CNT. The V_{th} shifted to more negative values as well, as shown in Figure 6.4B.

Overall, the magnitude of the changes in conductance and V_{th} were quite consistent from device to device, with the exception of the event shown in Figure 6.4C and D. The event shown in Figure 6.4C is exceptional in that there is a two-step drop in conductance. This could be due to the cell interacting with more than one CNT spanning the device, with each drop corresponding to an interaction with a different CNT or small group of CNTs. This would also explain the unusually large change in conductance (Figure 6.4C) and ΔV observed (Figure 6.4D).

According to (Heller, Janssens et al. 2008), the V_{th} shift observed in the suspended CNT experiments is indicative of molecules adsorbing to the CNT.

Presumably, the CNT is pushed into the cell membrane during the experiments, resulting in lipid and protein adsorption to the CNT. This could be one reason it takes many seconds for the observed conductance drop in the experiments. Time is needed for the cell to enter the trench and the CNT to move past the polar head groups of the membrane lipids into the hydrophobic core of the membrane. Additional evidence from lipid surfactant experiments (Richard, Balavoine et al. 2003) indicate that lipid molecules non-covalently bind to CNTs, presumably via hydrophobic interactions. Molecular Dynamics simulations of CNTs being pulled through lipid membranes also demonstrates retention of lipid molecules by the CNTs (Wallace and Sansom 2008). Because the conductance changes are irreversible upon removal of the cell, it is likely that membrane compounds remain attached to the CNT.

The event displayed in Figure 6.4E and F showing increases in conductance and V_{th} in response to cell contact is anomalous. This could possibly be due to a defect in the nanotube. The CNTs grown for these experiments typically function as p-type semiconductors. However, CNTs can also be n-type semiconductors or conductors. If the CNT that interacted with the cell behaved as an n-type semiconductor, then this may explain the positive shifts in conductance and V_g. Further experiments are needed to determine the mechanism of this type of response.

It is also possible that the cell membrane can be pushed further down such that the CNT passes into the cytosol of the cell. If the CNT were inside the cell, it may sense the cytosol potential, which is typically more negative than the surrounding bath solution. However it is unclear what effect the cytosol may have on the nanotube, since the CNT is hydrophobic it would presumably still be coated with lipids and membrane proteins. An interesting way to test this may be to control the voltage inside the cell using the whole-cell patch clamp technique (Sakmann and Neher 1995), where the interior of the cell is open to the micropipette it is attached to, and the potential

inside the cell is controlled via an electrode in the micropipette. If the CNT were in the cytosol it may sense changes in the intracellular potential of the cell.

The membrane potential may be the cause of the conductance shifts observed for the anomalous event shown in Figure 6.4E and F. If the CNT did somehow enter the cell cytosol the V_g sensed by the CNT would be shifted due to the cytosol potential, which is roughly -80 mV. This would shift the V_{th} to more positive values, which is what was observed in Figure 6.4F.

Conversely, the typical conductance change is a shift of V_{th} to more negative voltages. The shift is irreversible, i.e. it does not revert back to the original V_{th} when the cell is removed (Figure 6.4B). Therefore, the negative V_{th} shift observed suggests that the CNT is located inside the membrane, not the cytosol, and lipids and proteins are coating the CNT.

Evidence consistent with the idea that a lipid-coated CNT would loose its sensitivity to cell membranes comes from my efforts to image cells atop suspended nanotubes with TIRF microscopy. A report by Zhou, et al (Zhou, Moran-Mirabal et al. 2007) noted the observation of a dark line in a fluorescently labeled supported lipid bilayer at the location of the carbon nanotube in their device. Using TIRF microscopy and cells with fluorescently labeled membranes, we hoped to see similar results with the CNT devices used here, while simultaneously measuring device conductance.

This was attempted with two different lipophilic fluorescent labels, FM1-43 and DiI-C_{18}-3, as described in the *Methods* section. These labels both have long hydrophobic tail regions similar to lipids, and label cell membranes. Due to the poor imaging conditions caused by the trenches under the CNTs, it was impossible to detect any dark lines in contrast to the fluorescent membrane that may have been due to the presence of a CNT. Five conductance experiments were attempted with the FM1-43 cells for which the CNT positions were known from of the photocurrent images. This

should have resulted in several successful cell-CNT interactions. However, in the case of FM1-43 the label was present in the external buffer atop the CNT devices used. During the setting up of the experiments, the solution is in contact with the device coverslip for several minutes. This gives the relatively hydrophobic dye molecules in solution ample time to coat the hydrophobic CNTs, rendering them insensitive to the cells during the actual experiments. This effect was not observed with the DiI-C_{18}-3 labeled mast cells most likely because the mast cell buffer was replaced when the cells were obtained, washing away any excess dye molecules.

In summary, suspended CNTs can interact with cell membranes. The data suggests that the CNT typically incorporates into the hydrophobic core of the cell membrane, changing the CNT's conductance and V_g dependence in a measureable way. These experiments indicate that it may be possible to create biosensors to detect, via hydrophobic interactions, whole cells or measure changes in cell membranes due to proteins, toxins, viruses, permeablizing agents, etc. Functionalization of the CNTs may bring about even more versatility. Further characterization of CNT interaction with hydrophobic molecules, cells, and organelles will be needed and may open up opportunities to design novel biological sensor devices.

6.6 Acknowledgements

Thanks go to Qinghua Fang for the chromaffin cell culture, and Joan Lenz for excellent technical assistance. I thank Samantha Roberts for the many discussions about the experiments, encouragement in writing and critical reading of this chapter, and Paul McEuen for reviewing this chapter. This work was supported by the NBTC (NSF Agreement No. ECS-9876771) and NIH (RO1 NS38200, T32GM007469). It was performed in part at the Cornell Nanofabrication Facility which is supported by NSF Grant ECS-9731293, its users, Cornell University and Industrial Affiliates.

REFERENCES

Ahn, Y. H., A. W. Tsen, et al. (2007). "Photocurrent imaging of p-n junctions in ambipolar carbon nanotube transistors." Nano Letters **7**(11): 3320-3323.

Bachtold, A., P. Hadley, et al. (2001). "Logic circuits with carbon nanotube transistors." Science **294**(5545): 1317-1320.

Balasubramanian, K., M. Burghard, et al. (2005). "Photocurrent imaging of charge transport barriers in carbon nanotube devices." Nano Letters **5**(3): 507-510.

Bradley, K., A. Davis, et al. (2005). "Integration of cell membranes and nanotube transistors." Nano Letters **5**(5): 841-845.

Gruner, G. (2006). "Carbon nanotube transistors for biosensing applications." Analytical and Bioanalytical Chemistry **384**(2): 322-335.

Heller, I., A. M. Janssens, et al. (2008). "Identifying the Mechanism of Biosensing with Carbon Nanotube Transistors." Nano Letters **8**(2): 591-595.

Iijima, S. (1991). "HELICAL MICROTUBULES OF GRAPHITIC CARBON." Nature **354**(6348): 56-58.

Larrimore, L. (2008). Chemical and Biological Sensing with Carbon Nanotubes in Solution. Physics Department. Ithaca, NY, Cornell University. **PhD Dissertation**.

Larrimore, L., S. Nad, et al. (2006). "Probing electrostatic potentials in solution with carbon nanotube transistors." Nano Lett **6**(7): 1329-33.

Parsons, T. D., J. R. Coorssen, et al. (1995). "Docked granules, the exocytic burst, and the need for ATP hydrolysis in endocrine cells." Neuron **15**(5): 1085-96.

Richard, C., F. Balavoine, et al. (2003). "Supramolecular self-assembly of lipid derivatives on carbon nanotubes." Science **300**(5620): 775-8.

Rosenblatt, S., Y. Yaish, et al. (2002). "High Performance Electrolyte Gated Carbon Nanotube Transistors." Nano Lett. **2**(8): 869-872.

Sakmann, B. and E. Neher (1995). Single-channel recording. New York, Plenum Press.

Sazonova, V. (2006). A Tunable Carbon Nanotube Resonator. Physics Department. Ithaca, NY, Cornell University. **PhD Dissertation**.

Trojanowicz, M. (2006). "Analytical applications of carbon nanotubes: a review." Trac-Trends in Analytical Chemistry **25**(5): 480-489.

Wallace, E. J. and M. S. Sansom (2008). "Blocking of carbon nanotube based nanoinjectors by lipids: a simulation study." Nano Lett **8**(9): 2751-6.

Zhou, X., J. M. Moran-Mirabal, et al. (2007). "Supported lipid bilayer/carbon nanotube hybrids." Nat Nanotechnol **2**(3): 185-90.

CHAPTER 7

CONCLUSIONS AND FUTURE DIRECTIONS

Microfabricated devices have opened new doors to understand the mysteries of biological processes. By creating tools on the same scale as the biological process we are interested in, it becomes possible to detect some of the discrete steps in that process and in turn gain a better understanding of how that process works. And from there, to understand what happens when the biological process breaks down due to disease, toxins, genetic anomalies, and so forth. Armed with this knowledge, microdevices could again become useful for the detection and possibly treatment of illness.

In this work, the microscopic tools come in the form of microfabricated electrodes and photons. In chapter 3, I introduced planar amperometric electrode arrays that could be used in conjunction with fluorescence microscopy techniques. This combination allowed us not only to determine the location of exocytotic release events, but gain information about the release and diffusion kinetics of the process as well. This combination continues to prove highly useful, as can be seen in the extensions and applications of the concept in chapters 4 and 5.

A challenging future experiment using this technique involves using the four-electrode arrays in combination with TIRF microscopy to study SNARE protein conformational changes using Förster (or Fluorescence) Resonance Energy Transfer (FRET). In this experiment, two of the SNARE proteins would be labeled with specific fluorescent proteins such that when one protein's fluorophore is excited via TIRF excitation, if it is in close proximity to the second protein's fluorophore, the excitation energy will be transferred to the second fluorophore, where it is released as a photon at a longer wavelength then the first fluorophore would have. It should be

possible to correlate the locations of these changes to exocytotic locations derived from the electrode arrays, and gain information about how the SNARE proteins are behaving prior to, during, and perhaps after exocytosis.

In chapter 4, the electrode array concept was extended to transparent materials. Here I have shown that ITO, previously used in biology mainly in the study of action potentials from neural networks, can detect exocytosis directly from cells. Also, I have shown that Gold, traditionally an opaque material, can be made thin enough to be partially transparent while still maintaining its electrical properties. In the future, these properties could enable direct and simultaneous electrochemical and fluorescence detection of exocytosis in neurons – a nearly impossible task with current technology. Currently, one is limited to either fluorescence labeling techniques or electrochemical techniques. I believe it would be exciting and enlightening to see exocytotic events at neuronal synapses correlated with discrete fluorescence information. With this in mind, work has begun on a "neuron electrode array" consisting of a large number of transparent electrodes in a $1mm^2$ area. Glass (SiO_2) insulation would enable proteins or other molecules of interest to be patterned atop the arrays to direct cell growth and possibly synapse formation. Alternatively, this device could become a massively multiplexed detection array for other cell types or perhaps even drug screening.

The results of chapter 5 indicate that the transmembrane domain of synaptobrevin plays a significant roll in the exocytotic mechanism. An interesting future experiment would be to perform similar mutations to syntaxin, synaptobrevin's plasma membrane counterpart in the SNARE complex, to see if there are similar changes in the exocytotic mechanism. If this is the case, it could also imply that syntaxin and synaptobrevin are the true keys to the exocytotic mechanism, and SNAP-25 is just there to hold them in place and "zip" them up. Using the zipper analogy, think of synaptobrevin and syntaxin as the teeth on two sides of a zipper, and SNAP-

25 as the zipper pull. As SNAP-25 zips the other two proteins together, they exert forces on the plasma and vesicle membranes, possibly pulling their transmembrane domains into the lumins of their two respective membranes. This would act to bring the two membranes closer to one another and possibly disrupt the membranes with the movement of the protein transmembrane domains, leading to the formation of a fusion pore. The charged peptides placed at the C-terminus of synaptobrevin in the experiments of chapter 5 could disrupt this process by making it energetically unfavorable to pull the transmembrane of synaptobrevin into the vesicle membrane. Clearly more experiments are needed to test this hypothesis.

The goals of experiments presented in chapter 6 were more of a fundamental scientific nature then those of the previous chapters. It was shown for the first time that unmodified carbon nanotubes can sense the presence of and interact with cells. And, that it would appear that the nanotubes may become coated in lipids as they interact with the cells. These experiments are still ongoing, now mainly with giant unilaminar and multilaminar vesicles using a photocurrent microscope to detect changes in the nanotube band structure in the presence of these vesicles. These experiments will not only be relevant to biosensor applications, but a more fundamental understanding of carbon nanotube behavior in an aqueous environment.

Overall, these experiments have demonstrated new detection techniques utilizing planar electrode arrays and fluorescence microscopy to aid in the understanding of the exocytotic process and cell biology.